# INFLUENCE OF MICROSTRUCTURE ON THE PROPAGATION OF FATIGUE CRACKS IN INCONEL 617

by

Benjiman Michael Albiston

A thesis

submitted in partial fulfillment

of the requirements for the degree of

Master of Science in Materials Science and Engineering

Boise State University

December 2013

BOISE STATE UNIVERSITY GRADUATE COLLEGE

# DEFENSE COMMITTEE AND FINAL READING APPROVALS

of the thesis submitted by

Benjiman Michael Albiston

Thesis Title: Influence of Microstructure on the Propagation of Fatigue Cracks in Inconel 617

Date of Final Oral Examination: 10 July 2013

The following individuals read and discussed the thesis submitted by student Benjiman Michael Albiston, and they evaluated his presentation and response to questions during the final oral examination. They found that the student passed the final oral examination.

| | |
|---|---|
| Megan E. Frary, Ph.D. | Chair, Supervisory Committee |
| Michael F. Hurley, Ph.D. | Member, Supervisory Committee |
| Clyde J. Northrup, Ph.D. | Member, Supervisory Committee |
| Richard N. Wright, Ph.D. | Member, Supervisory Committee |

The final reading approval of the thesis was granted by Megan Frary, Ph.D., Chair of the Supervisory Committee. The thesis was approved for the Graduate College by John R. Pelton, Ph.D., Dean of the Graduate College.

ACKNOWLEDGEMENTS

This investigation was conducted as part of the requirements for the degree of Master of Science in Materials Science and Engineering from Boise State University. The material and instruments used in this investigation were provided or made available by the Department of Materials Science and Engineering at Boise State University and the Center for Advanced Energy Studies. This research was funded by the Idaho National Laboratory and the Department of Materials Science and Engineering at Boise State University, under the supervision of Dr. Megan Frary. I would like to acknowledge Dr. Megan Frary, as her guidance, support, and understanding made this thesis possible. In addition, the useful discussions and support provided by Dr. Mike Hurly were deeply appreciated. A special thanks to the faculty and staff at Boise State University for support and assistance in all facets of this research. Finally, thank you to my parents who encouraged and supported my goals in obtaining a higher education.

## ABSTRACT

Inconel 617 is a candidate material for use in the intermediate heat exchanger of the Next Generation Nuclear Plant. Because of the high temperatures and the fluctuations in stress and temperature, the fatigue behavior of the material is important to understand. The goal of this study was to determine the influences of the microstructure during fatigue crack propagation. For this investigation, Inconel 617 compact tension samples, fatigue tested by Julian Benz at the Idaho National Laboratory, were obtained. The testing conditions included two environments at 650 °C (lab air and impure-He) and varied testing parameters including: loading waveform (triangular, trapezoidal), loading frequency (0.01, 0.05 Hz), and maximum stress intensity factor, $K_{max}$ (20, 25, 30 MPa$\sqrt{m}$). The value of $K_{max}$ had the greatest influence in the crack growth rate followed by the testing environment. In this study, electron backscatter diffraction was used in order to relate the crack path to the microstructure on the scale of microns. Using this information the crack was found to crack in the {001} family of planes and <001> to the <112> family of directions with the least propensity to propagate in the <111> family of directions. This supports that crack growth in Inconel 617 at 650 °C propagates with a 'quasi-cleavage' mechanism. Also in this study it was found that the character of fatigue crack deflections within a grain versus that at a grain boundary differs with statistical significance. Within a grain, the deflection angle had a unimodal distribution with a mean of 16° ±15°. The low angle of deflection suggests that the plane of highest stress is the highest influencing factor. Also, the deflections at the grain boundary were found to

have a different distribution as it was multimodal, which suggests multiple mechanisms for fatigue crack deflection. Though, the fatigue crack growth rate was found to be highly influenced by the testing atmosphere and loading parameters, they were found to have no statistical significance on the fatigue crack path on the microstructural level. At these testing conditions, the crack grew at a rate slow enough for the microstructure to have influence on its path, though it was still constrained to remain close to the plane of highest stress. Developing a deeper understanding of the influence of microstructure on fatigue crack propagation will support selection of materials and design of the intermediate heat exchanger for the next generation nuclear plant.

TABLE OF CONTENTS

LIST OF TABLES

LIST OF FIGURES

# LIST OF ABBREVIATIONS

| | |
|---|---|
| ANOVA | Analysis of Variance |
| ASTM | American Society for Testing and Materials |
| ChI | Chemical-assisted Indexing |
| CSL | Coincident Site Lattice |
| CT | Compact Tension |
| EBSD | Electron Backscatter Diffraction |
| EBSP | Electron Backscatter Patterns |
| EDS | Energy-dispersive X-ray Spectroscopy |
| FCC | Face-centered Cubic |
| FIB | Focused Ion Beam |
| INL | Idaho National Laboratory |
| IPF | Inverse Pole Figure |
| IQ | Image Quality |
| OIM™ | Orientation Imaging Microscopy |
| SEM | Scanning Electron Microscope |
| VHTP | Very High Temperature Plant |

| | |
|---|---|
| XPS | X-ray Photoelectron Spectroscopy |

# CHAPTER ONE: INTRODUCTION

## 1.1: Motivation for Research

In May 2005, congress passed the Energy Policy Act of 2005, which established as law that the U.S. Department of Energy shall establish a Next Generation Nuclear Plant project [1]. This act stated that the project should develop and design a prototype reactor that has the capabilities to produce both electricity and hydrogen. Today the production of hydrogen is reliant on technologies that yield greenhouse gases, which the lowering of is a driving factor in our increasing need for $H_2$ [2]. Based on the above requirements, the Very High Temperature Reactor (VHTR) design was selected for the project. This would allow for the creation of electricity and hydrogen in a state-of-the-art, thermodynamically efficient manner without the creation of greenhouse gases [1]. However, the use of this technology introduces significant obstacles that need to be overcome before the project can be realized. One of the first considerations to be satisfied is the designed service life; this reactor is required to remain in service for 60 years. Therefore, understanding the interactions of the materials used in the manufacture of the plant with the environmental conditions is imperative. The data and models for current high-temperature alloys are inadequate and will be a significant focus of the project.

One concern with the VHTR is its upper temperature limit. The designed gas outlet temperature is 950 °C (reduced from 1000 °C) [1]. This is at the upper limit of

many metallic materials that are available today [1]. The high temperature incorporates significant mechanical and chemical mechanisms of degradation that must be understood and designed around. These include time dependent deformation (creep), cycle dependent deformation (fatigue), and corrosion. These processes are greatly influenced by the microstructure of the material. Understanding these interactions and the long-term stability of the microstructure are paramount to the success of the overall Very High Temperature Reactor project.

### 1.2: Research Objectives

Microstructural character plays an important role in the bulk properties of a material. Defects in structures are impossible to avoid during forming and joining of parts. Therefore, in a structure with a service life of 60 years, it is important to understand the implications of these defects and effects of the conditions within the intermediate heat exchanger. Fatigue crack growth within a material is important to investigate because if left undetected it can lead to catastrophic failure without any deformation process to serve as warning. The primary objective of this research was to study the relationship between microstructure and fatigue crack growth in Inconel 617 at high temperatures. The information gained from this research can be used in predictive models for the structural integrity of materials and can be used in design in order to optimize the material for application. The objective was approached from different aspects: crack propagation planes and directions within grains and the effect of grain boundaries on crack propagation.

# CHAPTER TWO: BACKGROUND INFORMATION

## 2.1: Inconel 617

The proposed candidate materials for the intermediate heat exchanger for the Next Generation Nuclear Plant are Inconel 617 and Haynes alloy 230. The operating conditions for the plant present challenges that must be overcome in materials selection. This includes withstanding temperatures up to 950 °C in helium for up to 60 years. For a material to qualify for implementation, there must be enough data on the mechanical properties for model development and codification under the American Society of Mechanical Engineers Boiler and Pressure Vessel Code. Both of the aforementioned alloys possess properties that allow for high temperature service with a good combination of high-temperature strength and oxidation resistance. However, as compared to Inconel 617, alloy 230 is relatively new and even though preliminary data suggests it can outperform Inconel 617, it does not have an established database of properties. This leads to Inconel 617 as the primary candidate material as it can be codified within the timeframe of the project [1].

Inconel 617 is a solid-solution strengthened nickel-based superalloy [3-6]. The alloy contains many constituents, shown in Table 1, used to improve its high temperature strength and corrosion resistance [3]. The solid-solution strengthening that increases the alloy's creep resistance is provided by chromium and molybdenum. From these, carbide precipitates form, with the chromium-rich primarily on the grain boundaries and

molybdenum-rich within the matrix [3]. The alloy is typically purchased in the solution annealed condition, although precipitation of carbides can occur during service [6]. High temperature corrosion is combated by the inclusion of aluminum and chromium along with the nickel, all of which form passive layers on the surface of the material [3]. Passivation of the bulk material effectively reduces the rate of corrosion; however, oxidation still plays an important part in the mechanical properties such as the fatigue resistance of the material. The interaction of oxygen along grain boundaries, micro-cracks, and in the matrix can have a detrimental impact on the overall service life and cost [4, 7-9].

**Table 1. Chemical composition of Inconel 617 (wt. %) [3]**

| ***Element*** | ***wt %*** |
|---|---|
| Nickel | 44.5 min. |
| Chromium | 20.0-24.0 |
| Cobalt | 10.0-15.0 |
| Molybdenum | 8.0-10.0 |
| Aluminum | 0.8-1.5 |
| Carbon | 0.05-0.15 |

### 2.2: Fracture Mechanics

Whether engineering an automobile, plane, or nuclear reactor, it is important to understand how a structural component will endure during its service life. Basic material properties can be used to determine safe service load limits, but an understanding of fracture mechanics will give insight into the stresses that a material can carry, with and without defects. How long can the part last, with and without defects? What is the confidence in your above answers?

Knowledge of the mechanics of crack growth along with its interactions with the microstructure can lead to the answers of the above questions. Interest in the field of

fracture mechanics developed as a result of World War II; failures of welded ships, gas-transmission lines, oil storage tanks, and pressurized cabin planes drove the need for research [10]. All structures contain defects such as voids, porosity, and surface defects introduced during manufacture and/or during the service life. These defects can be initiation points for cracks during cyclic loading. Fracture mechanics accesses the durability of materials and structural members that contain cracks or crack-like defects, determining at what loads cracks may grow [11, 12]. Understanding the fracture mechanics of a material and with the development of models, structures can be manufactured to enhance a safe service life while saving the cost of "over-engineering."

2.2.1: Linear Elastic Fracture Mechanics

Linear elastic fracture mechanics require linear-elastic behavior, which is usually only seen in brittle materials such as ceramics. However, it can be applied to ductile materials in the region near the crack tip. This allows for analysis of the elastic stress field near the crack tip, which is described by the stress intensity factor, K. At the crack tip, the model shows the stress as infinite and therefore neglected. The stress field near the crack tip in an infinitely extended plate is approximated by:

$$\tilde{\sigma}_{11}(r,\varphi) = \frac{K_I}{\sqrt{2\pi r}} \cos\frac{\varphi}{2}\left[1 - \sin\frac{\varphi}{2}\sin\frac{3\varphi}{2}\right] \quad (1)$$

$$\tilde{\sigma}_{22}(r,\varphi) = \frac{K_I}{\sqrt{2\pi r}} \cos\frac{\varphi}{2}\left[1 + \sin\frac{\varphi}{2}\sin\frac{3\varphi}{2}\right] \quad (2)$$

$$\tilde{\tau}_{12}(r,\varphi) = \frac{K_I}{\sqrt{2\pi r}} \cos\frac{\varphi}{2}\sin\frac{\varphi}{2}\cos\frac{3\varphi}{2} \quad (3)$$

where r and φ are polar coordinates centered at the crack tip, $\tilde{\sigma}_{11}$, $\tilde{\sigma}_{12}$, and $\tilde{\tau}_{12}$ are the approximate external applied stresses and $K_I$ is the stress intensity factor. In order for

this model to be used, the geometry of the specimen and crack length must be incorporated:

$$K_I = \sigma\sqrt{\pi a}\, Y \quad (4)$$

where 'a' is the half crack length. The 'I' subscript denotes mode I loading, which is one of three possible loading geometries. Mode I is a load normal to the crack plane; mode II is in the direction of crack propagation; and mode III is perpendicular to crack propagation but still in the crack plane. Finally, Y is a parameter, which is a function of specimen and loading geometry.

2.2.2: Griffith Fracture Strength Theory

Stability of cracks were first analyzed by Griffith in 1920 [13]. His postulate was that the stability of a crack under stress is a balance between the change in potential energy from the introduction of new crack surface and the introduced stress. Therefore, in order for a crack to propagate, the introduced stress at the crack tip must overcome the cohesive strength of the material and an increase in potential energy of the system.

To derive a generalized crack driving force using Griffith's theory [13], consider again an infinite plate. It will have a determined thickness of B, with a crack through this thickness of length 2a, have a uniform stress in both the x and y directions, and be of an elastic material. The potential energy of the system can be described by:

$$U = U_0 - U_a + U_\gamma \quad (5)$$

where U is the potential energy of the system, $\mathbf{U_0}$ = potential energy of the system before introducing the crack, $\mathbf{U_a}$ = the decrease in potential energy due to deformation accompanying crack formation, and $\mathbf{U_\gamma}$ = the surface energy associated with the

formation of new crack surfaces. Using the relationships for $U_a$ and $U_\gamma$ described by Inglis [14] in his 1913 paper the crack driving force can be found using:

$$G = \frac{\pi\sigma^2 a}{E} \tag{6}$$

where G is the elastic energy per unit area of crack surface made available for a small increment of crack extension.

### 2.3: Fatigue

It is important to understand what fatigue is and its mechanism. A system where a material is cyclically loaded at *less* than its tensile strength can lead to a weakening or catastrophic fracture, not preceded by a large plastic deformation [12].

There are three stages of damage evolution in the fatigue process: crack initiation, crack propagation, and catastrophic failure. Fatigue fracture starts at highly loaded positions within the material; the localized stress concentrations are often caused by notches, whether by design or defect. However, even if a component is "defect free," a crack can be initiated by surface roughening caused by plastic deformation [12]. This is caused from dislocation movement at stresses below the yield strength. Under cyclic loading, the small plastic deformations accumulate and initiate a crack. Figure 1 demonstrates how the movement of dislocations in slip systems can forms notches in an otherwise defect free material. These act as initiation points for fatigue cracks.

Figure 2 shows a crack growth rate curve. This can be used to explain the three regimes of crack growth. In region I, initiation of microcracks, which propagate on a plane close to that of the maximum shear stress, occur. It starts at the fatigue crack threshold, $K_{Th}$, which is defined as the point at which $da/dN$ approaches zero and

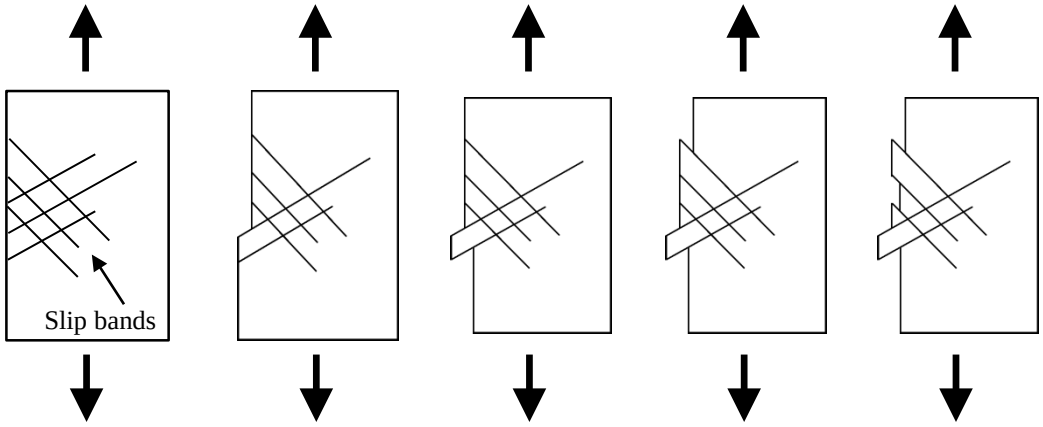


**Figure 1. The formation of intrusions and extrusions due to cyclic loading. The number of cycles increases from left to right.**

continues until the crack growth rate is nominally less than $10^{-5}$ mm/cycles [15]. Region III shows that increasing stress will cause the crack growth rate to quickly increase, leading to the crack becoming unstable and the part failing. Within region II, the nominal crack growth rate is between $10^{-5}$ and $10^{-3}$ mm/cycle [15]. This region is most important as the crack growth rate can be described by the Paris Law [16]:

$$da/dN = C(\Delta K)^n \tag{7}$$

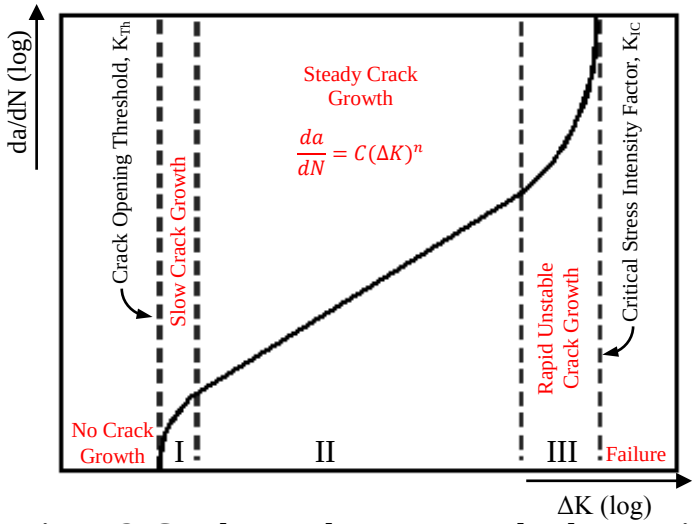


**Figure 2. Crack growth rate curve, the three regions of crack growth can be seen, with region II having a linear growth rate predicted by the Paris Law.**

where $da/dN$ is the crack growth rate per loading cycle and the right side of the equation has the range of the stress intensity factor, ΔK, and the material constants 'C' and 'n'. This model can be used in design to allow for fatigue cracking within the service life of the part with minimal risk of premature fracture. However, other considerations need to be made in this simple model because of the high temperature environment of the next generation reactor. For example, oxygen transport and oxidation have been shown to greatly affect the fatigue properties of a material [17-23].

### 2.3.1: Fatigue Crack Character

Deformation of a material when under a mechanical load is either elastic and reversible or plastic, which results in non-reversible changes within its microstructure. The movement of dislocations within the slip systems of the material accommodates plastic deformation. In face-centered cubic (fcc) materials, such as nickel, the slip systems are the $\{111\}$ family of planes and $\langle 1\bar{1}0\rangle$ family of directions.

The literature places fatigue cracks into two categories: short and long cracks [15, 24-26]. Short cracks can be further classified as microstructurally, mechanically, or physically short cracks [15, 26]. In microstructurally short cracks, the propagation rate is determined by interactions with the local microstructure [27]. The deformation zone ahead of the crack is relatively large compared to the crack length. As the crack increases in length to that of several grain diameters, the influence of the microstructure is greatly reduced. The transition from a microstructurally to a physically short crack is observed as the deformation zone becomes negligibly small ahead of the crack tip relative to its length [15].

Crack propagation is divided into two modes. These are related to, but should not be confused with, the stages of crack propagation seen in Figure 2. The modes of crack propagation are also related to, but differ from, the modes of loading a specimen. In this description of crack propagation, it is assumed that the 'loading mode' is always Mode I, normal tensile stress. In Mode I crack propagation, seen in stage II crack growth, the crack runs within the plane of maximum normal stress. In Mode II, seen in stage I crack propagation, the crack runs in slip planes most conveniently oriented relative to the maximum shear stress, approximately 45° from the direction of the normal stresses [15, 27]. This dependence on the orientation of slip planes with in the grain makes Mode II propagation dependent on its crystallographic orientation. The mode of crack propagation for microstructurally short cracks is mainly Mode II and the transition from Mode II to Mode I crack propagation helps define the transition to mechanically short cracks [26]. According to ASM, a crack is short so long as the radius of the deformation zone is greater than one-fiftieth of the crack length [15].

The evolution from physically short cracks to long cracks is defined by the complete development of plasticity-induced crack closure. Long cracks are typically greater than 0.5 mm in length and propagate in stage II type crack growth [15, 26]. Stage II crack growth occurs by transgranular fracture and the magnitude of the cyclic loading stress is of much greater influence than the average loading stress or microstructure [15, 26].

### 2.3.2: Factors Affecting Fatigue Crack Growth

Fatigue crack growth in nickel-based superalloys is affected by many parameters including the mechanical loading conditions, environment, and the microstructure

(further described below and in Section 2.3.3). The types of mechanical loading conditions include the loading frequency, waveform, stress intensity factor, and stress ratio [17, 28-31]. It has been found in many studies that the environment including temperature [32-38] and atmosphere [18, 39-43] plays a critical role in fatigue crack propagation in nickel-based superalloys. Many aspects of the microstructure influence the fatigue properties of a material. Studies show that secondary phases [38, 44, 45], grain size [46], grain orientation [47-51], and grain boundary character [48, 52-56] play an important role in the fatigue properties of nickel-based superalloys.

Studies on the effects of crystallographic orientation on fatigue crack growth have been performed. In a study performed on copper bi-crystals, it was found that the fatigue cracking is influenced by both the grain orientation and the relative orientation between the grain boundary and the primary slip systems [48]. It was found that as the angle between the grain boundary and primary slip system increased, fatigue crack initiation changed from within the grain to at the grain boundary [48]. Simonovski and Cizelj [51] showed that when short cracks extend from one grain into the next, they will change directions to follow the available slip plane in the next grain. Also, the closer the slip plane is to being perpendicular to the external load, the larger the crack tip opening displacement is [51]. Similar results were found in the nickel-based superalloy, Inconel 718 [57]. Andersson and Persson [57] found that with 1-3 mm cracks the crack growth was predominantly on slip planes in a shearing mode. The possible mechanism for this behavior is the formation of microcracks in the slip system ahead of the crack tip and the subsequent linking for causing growth of the fatigue crack [57]. In a study on a 3% silicon-iron alloy performed by Jono *et al.* [58], they found that the stress intensity factor,

K, influenced the number of slip systems activated during fatigue crack growth. In low K regions, only a single preferred slip system operated and the fatigue crack grew in a zigzag manner due to strain hardening [58]. In high K regions, two preferential slip systems operated simultaneously and the fatigue crack grew in a direction perpendicular to the loading axis [58].

Grain boundary character has also been shown to have influence on fatigue cracking. Li *et al.* [48] showed that grain boundaries with high interfacial energy tend to nucleate fatigue cracks sooner. In copper bi-crystals, it was found that cracks preferred to nucleate at high-angle boundaries [56]. In a study performed by Gao *et al.* [52], it was found that an engineered microstructure with a 40% increase of special boundaries, discussed later in this chapter, displayed only a marginal fatigue endurance increase while a fine grained (1.3 μm) versus a coarse grain (15 μm) microstructure saw a ~7% fatigue endurance increase. Grain boundaries were found to provide impedance to transgranular fatigue crack propagation; boundaries with higher misorientation tend to cause larger crack deflections [52].

### 2.3.3: Fatigue Cracking in Inconel 617

Inconel 617 is usually used in its solution annealed condition, but microstructural changes occur during its service life. Early on, chromium and aluminum oxide form on the surface, and long-term service will see inter- and intragranular carbides form [59, 60]. Also during aging, gamma prime forms in Inconel 617; this induces fatigue crack deflection, which shows a weakening effect for specimens [61]. The mode of fatigue crack propagation, intergranular or transgranular, in Inconel 617 is dependent on many factors. These were investigated in a study by Goswamii [44]. The strain rate can

determine the damage mode: at high strain rates fatigue crack propagation is transgranular, changing to intergranular with lower rates [44]. Similar trends were seen with dwell times in trapezoidal waveform fatigue loading. Larger dwell times (over 1 minute) produced intergranular cracking while short dwell times produced transgranular cracks [44].

The environmental effects on the fatigue properties of Inconel 617 have also been investigated. Kim *et al.* [62] investigated high temperature aging in an impure-He atmosphere. They found that the room temperature ductility of Inconel 617 was gradually lost with aging. It was proposed that intergranular oxides below the surface oxide layer and the coarsening of carbides on the grain boundaries were the cause of the loss of ductility. With the loss of ductility, the fracture mode was predominantly intergranular [62]. In a study performed by Totemeier and Tian [43], fatigue testing was performed in air, vacuum, and purified argon. In all environments, the introduction of a tensile hold period (trapezoidal waveform) reduced the fatigue life [43]. Fatigue lives were found to be longer in inert environments than in air [43].

### 2.4: Electron Backscatter Diffraction

Electron backscatter diffraction (EBSD) in the scanning electron microscope is increasingly used as a tool for characterizing the microstructure of engineering materials. This analysis technique allows for determination of microstructural information such as individual grain orientations, local texture, and phase identification, along with information such as stored energy or presence of plastic deformation [63-71].

In 1928, Nishikawa and Kikuchi observed the first diffraction pattern in backscattering mode [72]. In their experiments, the images from backscattered electrons

were obtained on a recording film placed in front of the specimen. This early technique was dubbed "high-angle Kikuchi diffraction" and is the basis of today's automated electron backscatter diffraction. Due to the wide spread availability of scanning electron microscopes (SEM) and today's computing power, this simple technique that could only characterize single points in a material can be used today to produce data on a square millimeter of material with a resolution below a micron in just a few hours. Today, with the introduction of the duel beam SEM/focused ion beam (FIB), three dimensional models of materials can be made.

Electron backscatter diffraction is an invaluable analytical method. There are many other tools including but not limited to transmission electron microscopy (TEM), X-ray Photoelectron Spectroscopy (XPS), and Raman spectroscopy that can give similar information on the structure and/or chemical composition of the specimen. However, no other technique can characterize the macrostructure of the material with micro-precision.

Electron backscatter diffraction patterns, as seen in Figure 3, are produced on a phosphor screen by high-energy electrons diffracted from the interaction volume of the

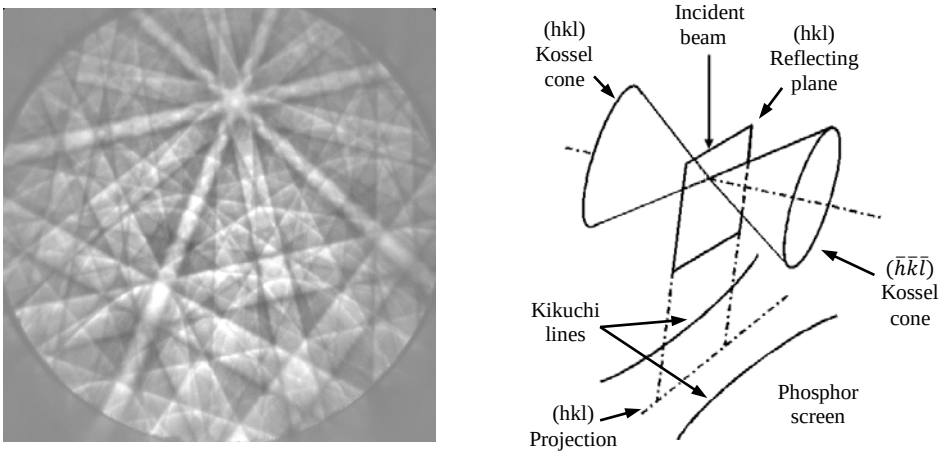


**Figure 3. Left: Backscatter Kikuchi patterns from Inconel 617. Right: Schematic of the kossel cones with respect to the reflecting plane, incident beam, and the phosphor screen.**

electron beam from the SEM within the specimen [63, 70, 71]. The light colored Kikuchi bands seen in the figure are the result of the diffraction from a single crystal. Intersections of the Kikuchi bands represent distinct zone axes. The relation between the incident electron beam, diffracting plane within the tilted specimen, and the phosphor screen is seen in the left image of Figure 3. In an electron backscatter diffraction (EBSD) experiment, the sample is placed in the SEM with a 70° tilt with respect to the incident electron beam. Electrons that interact with the material will be scattered toward the phosphor screen because of the sample tilt. The width of the line is developed from electrons passing on either side of diffraction point. This produces a cone, called a Kossel cone, which produces lines instead of the typical diffraction spots seen in TEM experiments. The Kikuchi pattern is the gnomonic projection of the lattice on a two dimensional surface. The center point of the incident electron beam on the surface of the specimen is the center of the related Kikuchi pattern. Edges of the Kikuchi band relate to diffraction from the same set of planes within the interaction volume of the beam. Multiple theorems are needed to fully describe Kikuchi patterns. However, for basic crystallographic orientation determination, Bragg's law will suffice. The angles between the Kikuchi lines correspond to the interplanar angles while the width of the band is related to interplanar spacing, $d_{hkl}$.

$$2d_{hkl} \sin(\theta) = n \lambda \quad (7)$$

In order maximize the amount of information that can be obtained from EBSD, a dynamic model is needed. As mentioned above, Bragg's law can describe the network of Kikuchi bands but a dynamic theory is needed to describe its intensities.

The spatial resolution of the electron backscatter diffraction is dependent on many variables including the specimen material itself. The resolution differs in the x and y axes, because the diffraction patterns are produced from the interaction volume of the electron beam, and the sample is tilted 70°. With the proper parameters, the spatial resolution of copper is better than 0.05 microns, using a tungsten filament or 0.02 microns with a field emission gun [63].

Indexing Kikuchi patterns developed from electron backscatter diffraction is similar to indexing a traditional diffraction pattern. The separation between two adjacent Kikuchi lines is analogous to the separation between two (hkl) diffraction spots. Therefore, the Kikuchi lines can be indexed in much the same way. First, consider two different Kikuchi lines from the planes ($h_1k_1l_1$) and ($h_2k_2l_2$). The separations between their pairs of excess and deficit lines, $p_1$ and $p_2$, are in the ratio [73]:

$$\frac{p_1}{p_2} = \frac{\sqrt{h_1^2+k_1^2+l_1^2}}{\sqrt{h_2^2+k_2^2+l_2^2}} \tag{8}$$

The angle between two pairs of intersecting Kikuchi lines are also analogous to the angle between the corresponding diffraction spots, just as long the Kikuchi lines are not far from the center of the pattern [73]. Since the Kikuchi lines are a two dimensional representation of a three dimensional cone (Kossel Cone) emitted from the point of diffraction, the line will curve if too far from the center.

$$\theta_{hkl} = \sin^{-1}\left(\frac{\lambda}{2a}\sqrt{h^2+k^2+l^2}\right) \tag{9}$$

Using the ratio $\frac{p_1}{p_2}$ and $\theta_{hkl}$ the orientation of the crystal can be determined from a lookup-table that relates this information.

With today's technology, computers perform automated indexing of up to 450 patterns per second. In order to detect and digitize the Kikuchi bands, a Hough transform is applied [74]. The now digitized bands are compared to a look-up table generated from the known material parameters. A voting scheme is used to determine which crystallographic orientation or even which phase is currently producing the pattern [63, 75]. With this technology, what took days can take only a fraction of a second to complete.

2.4.1: Interpreting EBSD data

There are multiple means to extract meaning from EBSD data, including displaying properties in the form of maps as seen in Figure 4. The most common is the inverse pole figure (IPF) map (the left most illustration). This map is made of individual color-coded points where each shows sample direction relative to the crystal reference frame. The legend is a unit triangle with a color designated for each point or crystallographic direction. The use of the triangle is possible in cubic materials since the rest of the inverse pole figure shows redundant symmetrical points.

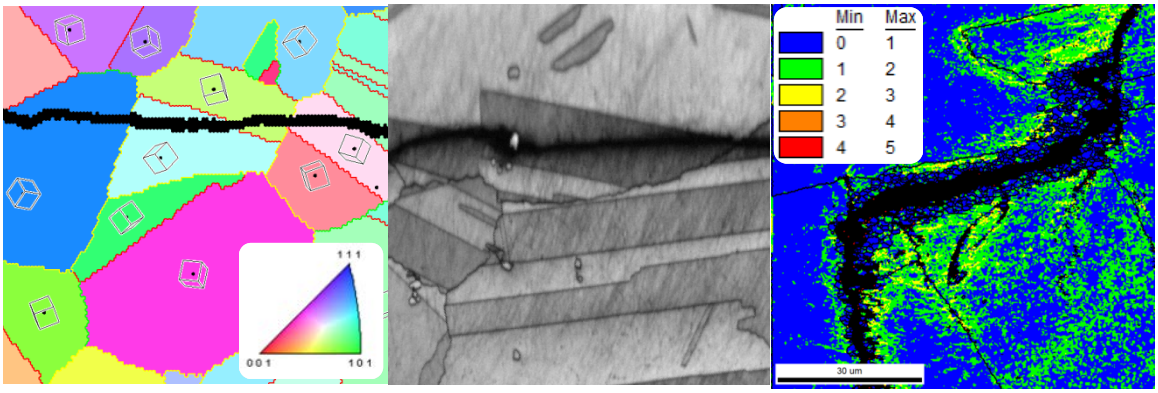


**Figure 4. Using maps is the most common means to interpret EBSD data. Left: Inverse pole figure (IPF) map. Each color represents a crystallographic orientation as seen in the legend. Center: Image Quality (IQ) map. Each point represents the 'quality' of the electron backscatter pattern. Lighter shows higher quality while darker is lower. Right: Average misorientation Map. Each point is represented by its average misorientation from its neighbors from 0-5°**

A second type of map is an image quality (IQ) map. This displays the 'quality' of the electron backscatter pattern (EBSP), as seen in Figure 5, at each pixel the gray scale represents the relative quality of the EBSP, where black is the lowest and white is the highest. The quality can depend on many factors including surface defects and

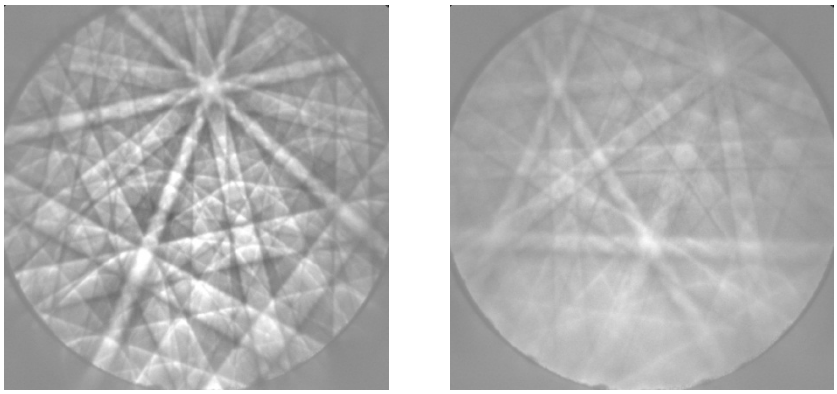

**Figure 5. These are electron backscatter diffraction patterns (EBSP) obtained from Inconel 617. Left: Shows a pattern with a high image quality. Right: Pattern with a low image quality.**

microstructural elements, thus it is not comparable between multiple scans but can be used to identify features in the microstructure. Examples of features that can be identified on an IQ map are grain boundaries, precipitates, and differing dislocation densities. Because the electron beam has an interaction volume within the material being analyzed, as it approaches a grain boundary, EBSPs for the grains on either side are produced. This lowers the overall 'quality' of the displayed pattern, thus showing the grain boundaries on the map. Overall dislocation density is shown in a similar manner, instead of patterns from multiple grains being produced, the pattern is disrupted by interactions with the dislocations [76]. Thus, a higher dislocation density will lower the image quality. The quality of the diffraction patterns is not only affected by the crystal lattice, but also by the material itself. Elements with higher atomic numbers typically produce stronger patterns. Therefore, scans with multiple phases containing differing elements will show a contrast in the IQ map [71].

Average misorientation maps are a means to identify strain in the lattice of the material being investigated. Local variations in misorientation of the crystal are a good indicator of strain. Each point in this map represents the average misorientation between it and all of its neighboring points to a defined nearest neighbor. The values will be between 0 and 5 degrees as a grain boundary is defined as a misorientation greater than 5 degrees [63].

### 2.4.2: Grain Boundary Character

It was generally believed until the 1930's that all grain boundaries were similar in nature and that an amorphous layer cemented individual grains together [77]. In the intervening years, a more sophisticated knowledge of grain boundaries has developed. The interfacial region between grains can have varying properties such as energy [77, 78], chemical reactivity [77, 78], and mechanical properties [77-79]. These properties are linked to the misorientation between the two grains. Description of this misorientation requires five parameters: three describe the misorientation between the grains and two describe the grain boundary plane [80, 81]. In order to simplify the classification of grain boundaries, it is generally accepted to separate them into 'general' and 'special' boundaries, where 'special' boundaries exhibit 'special' behavior [79, 82]. Special boundaries exhibit desirable properties, which are usually dramatically different from those of general boundaries such as boundary diffusion, boundary migration, and corrosion resistance [83, 84]. Those properties are correlated with the high degree of atomic matching found between grains with special boundaries [82-84]. The atomic matching of special boundaries can be found in low angle grain boundaries (those with a misorientation below 15°) and certain high angle boundaries, which exhibit grain

boundary energies, which are comparable to low angle boundaries [83]. The latter boundaries can be described by the coincident site lattice model [82, 85]. This binary approach to grain boundary classification aides the researcher in simplifying the effects of high versus low-atomic mismatch grain boundaries.

The coincidence-site lattice (CSL) model allows for correlation of the special properties with the existence of a periodic well-ordered intergranular area or super lattice [86]. In this model, lattice points that are in common with both lattices are identified. The CSL is characterized by the coincidence index ($\Sigma$), in which $1/\Sigma$ represents the fraction of lattice points common to both lattices [86]. For example, the $\Sigma 3$ twin boundary has a misorientation of 60°, but one in three lattice points are common between the two grains. Though there is a high degree of misorientation, the high atomic matching between the grains means this boundary will often be a low energy boundary [84, 86].

# CHAPTER THREE: EXPERIMENTAL METHODS

## 3.1: Specimen

Specimens were received from the Idaho National Laboratory (INL). Fatigue crack growth testing had been performed at INL on each sample. The Inconel 617 specimens were received in the compact tension (CT) form with the dimensions given in Figure 6. The specimens were cut from a plate of Inconel 617 obtained from Thyssen

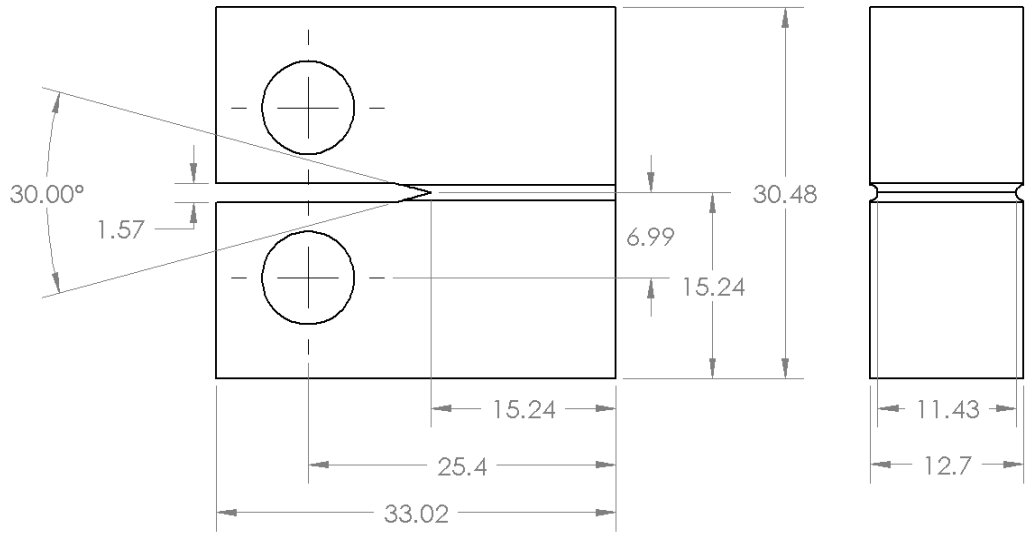


**Figure 6. Dimensions of the CT specimens received from the Idaho National Laboratory. All dimensions are in millimeters unless otherwise noted.**

Krupp VDM USA Inc (Florham Park, NJ). The chemical composition of the plate from the certification sheet is given in Table 2. The plate conforms to the specification ASTM B 168-08 and is in the solution annealed condition.

**Table 2. Chemical composition of Inconel 617 used in this study.**

| *Element* | *wt. %* |
|---|---|
| Nickel | 54.1 |
| Chromium | 22.2 |
| Cobalt | 11.6 |
| Molybdenum | 8.6 |
| Iron | 1.6 |
| Aluminum | 1.1 |
| Titanium | 0.4 |
| Manganese | 0.1 |
| Silicon | 0.1 |
| Carbon | 0.05 |
| Copper | 0.04 |
| Sulfur | < 0.002 |
| Boron | < 0.001 |

### 3.2: Fatigue Crack Growth Testing

The mechanical testing was performed by the INL. The tests were performed according to the ASTM E647-08 standard. Each sample was tested in a controlled environment where both atmosphere and temperature are held constant during the fatigue test. Each experiment uses multiple tests segments, given in Table 3, with varying parameters including $K_{max}$, waveform, and frequency.

Two atmospheres were used in testing. The first was so-called “lab air” while the second was impure-helium, concocted to simulate the atmosphere expected within the primary loops of the next generation nuclear reactor. The composition of the gas was 352 ppm H, 53 ppm CO, 10 ppm $H_2O$ vapor, with the balance being He. The INL study used multiple temperatures, but this work only considers tests performed at 650 °C. Because of the cost and availability of samples, this study focuses on two samples: one tested in lab air and the other in impure-helium.

**Table 3. Mechanical testing parameters of each test segment of the two specimens. For the trapezoidal waveform, the information in the frequency column is in the form: ramp up (s) - ramp down (s) - hold time at $K_{max}$ (s).**

**Specimen 1 (Lab Air Atmosphere; 650 °C)**

| *Increment #* | $K_{max}$ | *Waveform* | *Frequency (Hz)* |
|---|---|---|---|
| 1 | 20 | Sine | 1 |
| 2 | 25 | Sine | 0.5 |
| 3 | 25 | Triangle | 0.5 |
| 4 | 25 | Sine | 0.1 |
| 5 | 25 | Triangle | 0.1 |
| 6 | 30 | Triangle | 0.1 |
| 7 | 30 | Triangle | 0.05 |
| 8 | 30 | Trapezoidal | 10-10-10 |
| 9 | 30 | Trapezoidal | 10-10-60 |
| 10 | 30 | Trapezoidal | 10-10-300 |

**Specimen 2 (Impure-He Atmosphere; 650 °C)**

| *Increment #* | $K_{max}$ | *Waveform* | *Frequency (Hz)* |
|---|---|---|---|
| 1 | 19 | Triangle | 1 |
| 2 | 20 | Triangle | 0.5 |
| 3 | 20 | Triangle | 0.1 |
| 4 | 20 | Triangle | 0.05 |
| 5 | 20 | Triangle | 0.01 |
| 6 | 25 | Triangle | 0.5 |
| 7 | 25 | Triangle | 0.1 |
| 8 | 25 | Triangle | 0.05 |
| 9 | 25 | Triangle | 0.01 |
| 10 | 30 | Triangle | 0.5 |
| 11 | 30 | Triangle | 0.1 |
| 12 | 30 | Triangle | 0.05 |
| 13 | 30 | Triangle | 0.01 |
| 14 | 30 | Trapezoidal | 10-10-10 |
| 15 | 30 | Trapezoidal | 10-10-60 |
| 16 | 30 | Trapezoidal | 10-10-300 |

## 3.3: Microstructural Analysis

### 3.3.1: Specimen Preparation for EBSD Analysis

In order to perform microstructural analysis, the machined grooves on both faces of the samples, which contain the crack, had to be removed. The as-received sample configuration is seen in the left image of Figure 7. Surface material was removed using

120 grit SiC paper on a Buehler (Lake Bluff, IL) EcoMet® 3000 grinder-polisher. The right image in Figure 7 shows the sample with the groove removed and polished to a 600 grit finish. Though it is unseen to the naked eye, there is a 7-8 mm crack present on the surface of the sample in the right image. After removal of the machined grooves, the

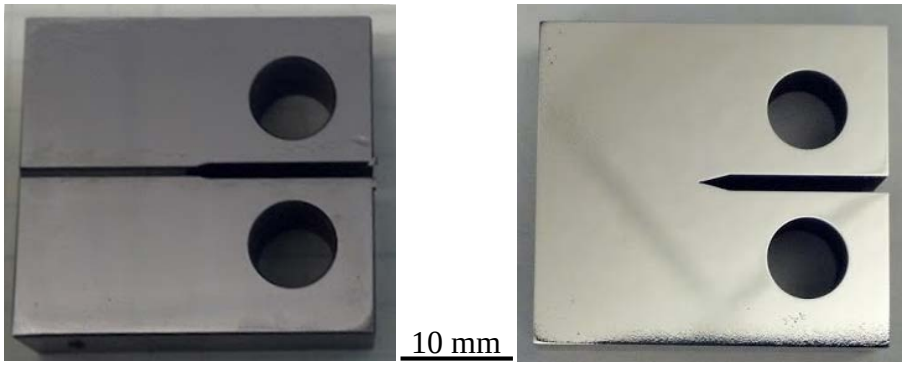


**Figure 7. Left: Image of the as-received sample from Idaho National Laboratory. Right: The sample prepared for analysis after the groove is removed through mechanical polishing.**

sample preparation procedure includes grinding in steps between 120 to 1200 grit SiC papers. This is followed by a final polish in a Bueler (Lake Bluff, IL) Vibromet 2® vibratory polisher with 0.05 μm alumina slurry for 36 h. The extended vibratory polish time was used in lieu of a final electrochemical etch in preparation for EBSD analysis.

In order to increase the area for analysis, multiple replications of EBSD data were taken from each side of both samples. After each analysis, approximately 500 μm were removed from the sample surface with 120 grit SiC paper. The surface was then re-prepared and EBSD scans of the newly exposed crack were obtained.

After all of the data collection iterations were completed, the sample was broken in two pieces in order to expose the crack surface. This allowed for confirmation of the crack length data obtained during mechanical testing by comparing it to the "beach-marks" formed by the change of testing parameters between each test segment. This

procedure allowed for direct correlation between the location of a point in the EBSD data and the mechanical test parameters.

### 3.3.2: EBSD Data Collection Procedure

Electron backscatter diffraction (EBSD) analysis was performed on a JEOL (Peabody, MA) JSM-6610LV scanning electron microscope (SEM) equipped with an EDAX (Mahwah, NJ) Hikari XP EBSD camera and an EDAX (Mahwah, NJ) TEAM™ EDS Analysis System. The scans were performed at the Center for Advanced Energy Studies (CAES). The EBSD scans with simultaneous energy-dispersive X-ray spectroscopy (EDS) were performed at 25 kV accelerating voltage, a step-size between 0.5-2 μm, and a scan area of approximately 300 μm x 1000-3000 μm. Scans were taken from the crack initiation point to its terminus. The data was collected and indexed using EDAX/TSL Orientation Imaging Microscopy (OIM™) Data Collection software version 6.2.

During the original data collection, a nickel phase material file was used for indexing, which allowed for the maximum data collection rate. The EBSD data was then rescanned using the Chemical-assisted Indexing (ChI) scan feature within the EDAX/TSL OIM™ Data Collection software. This method combines crystallographic data obtained from EBSD with composition data obtained from simultaneous EDS in order to differentiate between multiple phases during a scan. During this re-scan, molybdenum carbide, chromium carbide, and titanium carbide phases are included in addition to the nickel phase.

3.3.3: EBSD Data Cleanup Procedure

Before analysis of the EBSD data can be performed, data points that were not properly indexed during data collection must be evaluated to determine whether they are part of the crack or if they should be included within an adjacent grain. This was performed with the EDAX/TSL OIM™ Analysis software version 6.2. Two different approaches are used in determination of the crack location versus non-indexed data points. The built in cleanup algorithms included within the software were used.

The first cleanup algorithm used was the neighbor orientation correlation, which tests two conditions to determine if the orientation of a data point should be changed. The first condition compares each data point to its surrounding points determining if its orientation differs from its immediate neighbors. Depending on the cleanup level chosen (level 0-5), the data point must differ from all neighbors for level 0 to one neighbor for level 5. If the first condition is satisfied, then the algorithm compares the neighbors with each other to determine the numbers that have similar orientations within a tolerance. For level 0 all must have similar orientation, and for level 1, all but one must have similar orientations, up to level 5. If the two conditions are satisfied, the data point's orientation is randomly changed to that of one of its neighbors, which satisfies both conditions. For the selected cleanup level, the lower levels are performed first. This study used up to three iterations of the level 3 neighbor orientation correlation cleanup.

The second algorithm performed was grain dilation represented in Figure 8. This is only performed on data points that are not assigned to a grain. This is either from the point not being indexed or one that belongs to a group of points that are under the minimum grain size threshold. If a majority of the data point's neighbors belong to the

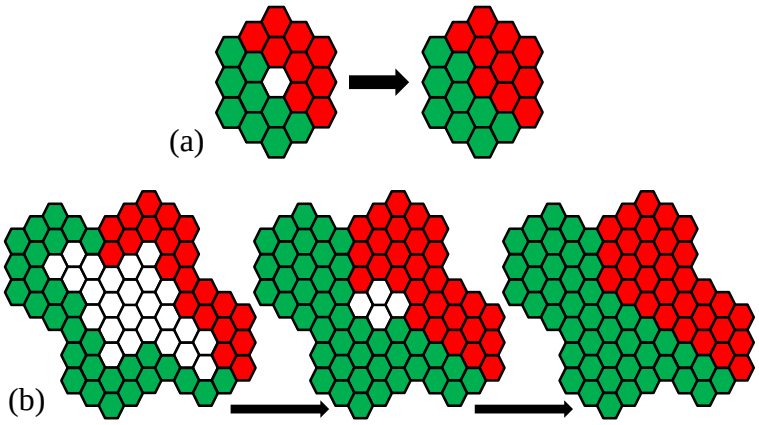


**Figure 8. (a) Example of grain dilation. The white data point is not associated with either grain. It is randomly assigned to a bordering grain. (b) Shows multiple iterations of grain dilation. Each point adjacent to a grain is assigned to that grain. This is repeated until all points are assigned.**

same grain, the point's orientation is changed to that of the majority grain. If not, the orientation is changed randomly to one of its neighboring grains. This algorithm can be performed in a single or multiple iterations, where in the latter the algorithm is repeated until each data point is assigned to a grain.

The cleanup procedure for the bulk microstructural analysis included up to three iterations of neighbor orientation correlation and a single iteration of grain dilation. For the crack propagation analysis, the grain dilation cleanup algorithm is changed to multiple iterations and two additional cleanup steps are added. The multiple iterations of grain dilation allows for the areas represented within the crack to be included in the grain in which it traverses, which "re-connects" the grains in order to simulate the original microstructure. Figure 9 shows the steps from raw data to cleaned up data with the crack shown.

It is assumed that before fatigue testing the bulk microstructure was strain free, therefore, there would be little orientation change within a single grain. During bulk

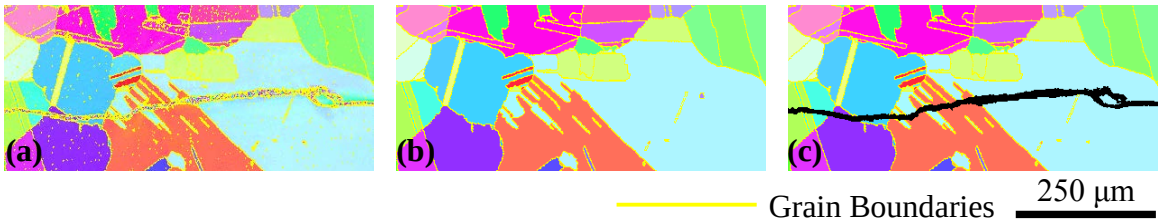


**Figure 9. IPF maps obtained during the data cleanup steps. (a) The raw data. (b) After the grain dilation and averaging cleanup steps. (c) Crack shown using the IQ threshold filtering.**

microstructural analysis, this was found to be true with only a small misorientation field located on either side of the crack. With this in mind, the single (average) orientation per grain cleanup algorithm, was used to simulate the pre-test microstructure. In this algorithm all orientation measurements within a grain are averaged and then replaced with the average, resulting in the grain having a single orientation.

The final step in the cleanup for crack propagation analysis was to differentiate the points located within the crack from those located in the bulk microstructure. This was accomplished by making a new data partition in which an image quality threshold was used to separate the two types of points. Figure 10 contains a histogram of the image

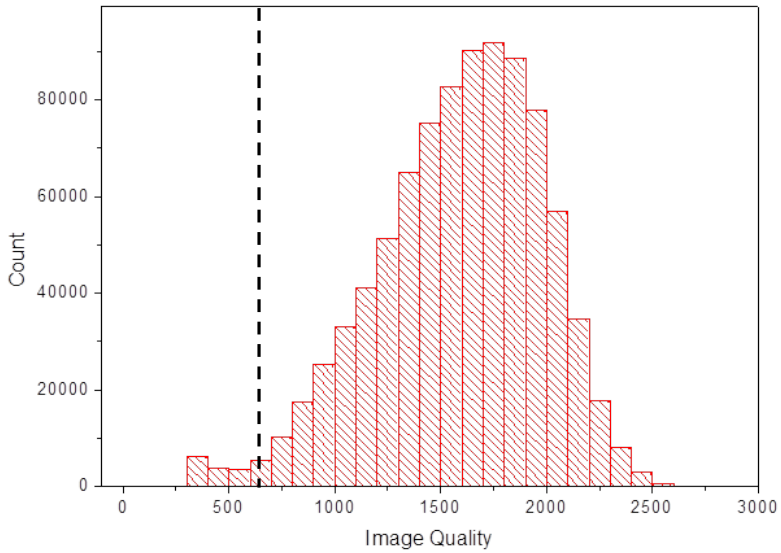


**Figure 10. Histogram of the Image Quality for an EBSD map. The black dashed line represents the location of the IQ threshold.**

quality of each point in a EBSD map, which was used to determine the image quality threshold used for the new partition. The intersection of the tail at the lower image quality and the "normal" distribution was used for the threshold. The example in Figure 10 would have an image quality threshold of approximately 700.

### 3.3.4: Analysis of Direction of Crack Propagation

To determine the effect of microstructure on crack propagation direction, the path of crack propagation in relation to the microstructural orientation was measured. It is assumed that the crack is a two dimensional plane that is perpendicular to the surface of the sample. Therefore, the crystal direction tool in the OIM™ Analysis software was used to determine the direction of crack propagation with in the grain. The dataset was first cleaned with the multi-iteration grain dilation and grain averaging steps. Before analysis, a data partition was formed with an image quality threshold in order to differentiate the crack from the microstructure. With these steps complete, an inverse pole figure map was used in conjunction with the crystal direction tool. The starting point for the tool is alongside the crack within the grain in question and the terminus is a point that allows the vector to be parallel to the section of crack being analyzed, as represented by the orange arrow in Figure 11. This procedure is repeated for the entire length of the crack for each determinable straight section. In this study, 5,299 data points were obtained for analysis.

The data obtained from the OIM™ Analysis crystal direction tool can be seen in the orange dashed inset in Figure 11. It includes the following information from the origin of the vector: orientation of the grain, the (x,y) coordinates within the map, the phase, and the grain ID (an unique number given by the software to identify the grain).

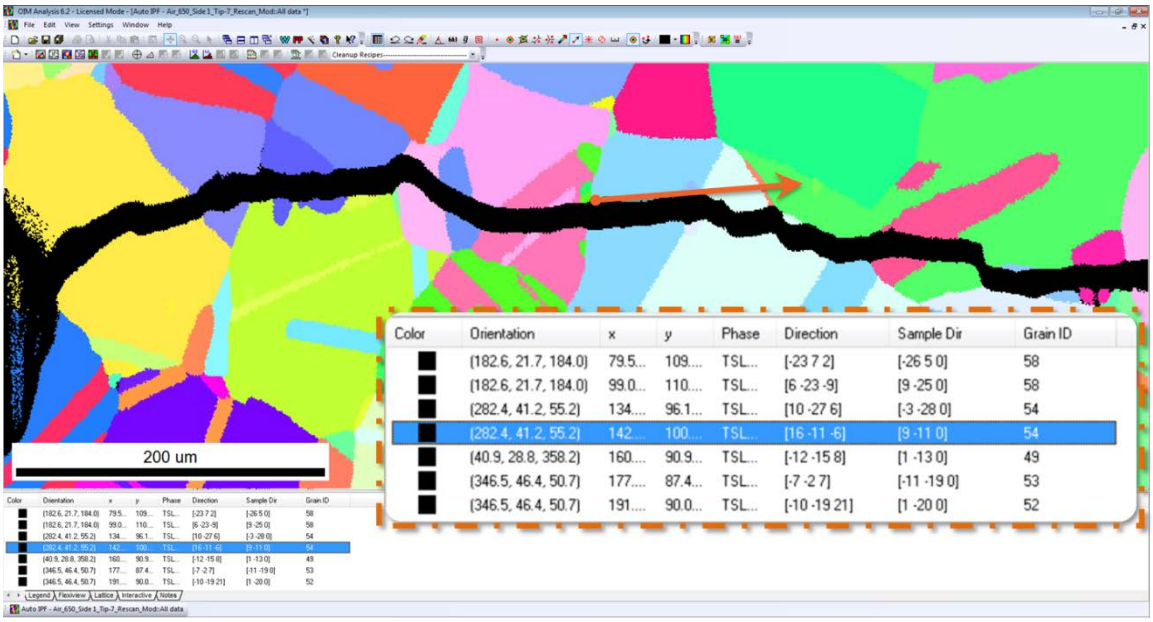


**Figure 11. Screenshot of the EDAX/TSL OIM™ Analysis 6.2. The image includes an inverse pole figure map of a dataset post-cleanup. The arrow represents use of the OIM™ crystal direction tool, where the dot is the start within the grain in question and the arrow point is the terminus lining up the crack propagation direction within the grain. The orientation data is given below the map, enlarged in the dashed inset.**

The data also includes information on the vector. The "sample direction" is the Miller indices for the direction of the crack within the sample reference frame, while the "direction" is the Miller indices within the reference frame of the grain

For analysis, the Miller indices for the crack propagation within the grain reference frame were converted to a point in inverse pole figure (IPF) space using Wolfram (Champaign, IL) Mathematica® 9.0. This allowed for visualizing the data in a unit triangle of an inverse pole figure where the direction of crack propagation is represented by the position of the point and other attributes such as grain size, phase, or testing parameters which are represented by size and/or color of the point.

3.3.5: Analysis of Change in Crack Propagation Direction

To determine the influence of grain microstructure and boundaries in the deflection of the fatigue cracks, the second approach analyzed the change in crack propagation direction and the parameters present during deflection. Similar to the previous analysis, the OIM™ Analysis crystal direction tool was employed. However, this analysis focused on sections of the crack that had a definable direction before and after a direction change. To perform the analysis, two vectors were made for each viable data point, 776; such points were measured in this study. As seen in Figure 12, the first vector is parallel to the crack propagation after the direction change (green arrow), while the second is parallel to the crack propagation direction before the path change (red arrow). Both vectors must be in within the same grain for the data to be comparable even if the change in propagation direction occurs at a boundary. Data similar to the first

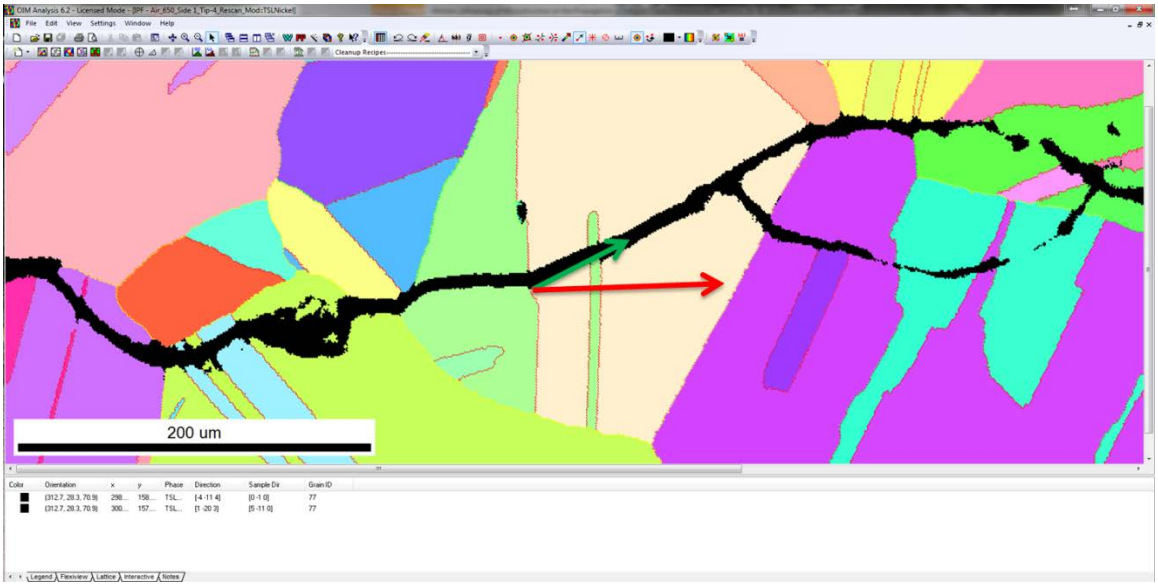


**Figure 12. Screenshot of the EDAX/TSL OIM™ Analysis 6.2. The image includes an inverse pole figure map of a dataset post-cleanup. The arrows represents use of the OIM™ crystal direction tool, where the green arrow is the direction of crack propagation within the grain in question and the red arrow the direction the crack propagation changed from (both arrows need to be within the same grain to be comparable).**

method is collected for each point with the addition of the environment where the direction changes occurred (e.g., within a grain or at a boundary). If at a boundary, it is noted whether it is a phase boundary or grain boundary and the character of the boundary. After the data is collected from the OIM™ Analysis software, the data is then analyzed using Wolfram Mathematica® 9.0 to determine the angle between the two vectors. The Mathematica® 9.0 notebook was also used to determine significance of the data using an analysis of variance, ANOVA.

# CHAPTER FOUR: RESULTS

## 4.1: EBSD Results and Statistics

Multiple sets of EBSD scans of each sample were obtained for analysis. The overall length of the crack in the impure-helium and lab air samples was 5.244 mm and 7.638 mm, respectively. Table 4 contains data on the length of the crack in each sample and the number of grains traversed. A total of 62.20 mm of overall crack length that traversed a total of 1,461 grains was investigated. This accounts for 64 hours of EBSD scan time.

**Table 4. Length of crack analyzed and the number of grains the crack traversed.**

| | **Impure-He** | **Lab Air** | **Total** |
|---|---|---|---|
| **Length of Crack** | 31.65 mm | 30.55 mm | 62.20 mm |
| **# of grains traversed** | 774 | 687 | 1461 |
| *33,314,134 data points & 64 hours of scan time* | | | |

In Figure 13 - Figure 22, the EBSD results for each dataset can be found. In each figure, the top image is a collage of image quality maps of the crack from initiation point to terminus. The images below are inverse pole figure (IPF) maps of the same. In the IPF maps, the grain boundary character is separated into three types: general, CSL (Special) and Σ3 boundaries. There are 6 sets of maps for the impure-helium sample (three iterations on each side) while there are only two iterations (1 & 3) for the lab air sample; the second iteration did not produce high enough quality kikuchi patterns for high confidence indexing.

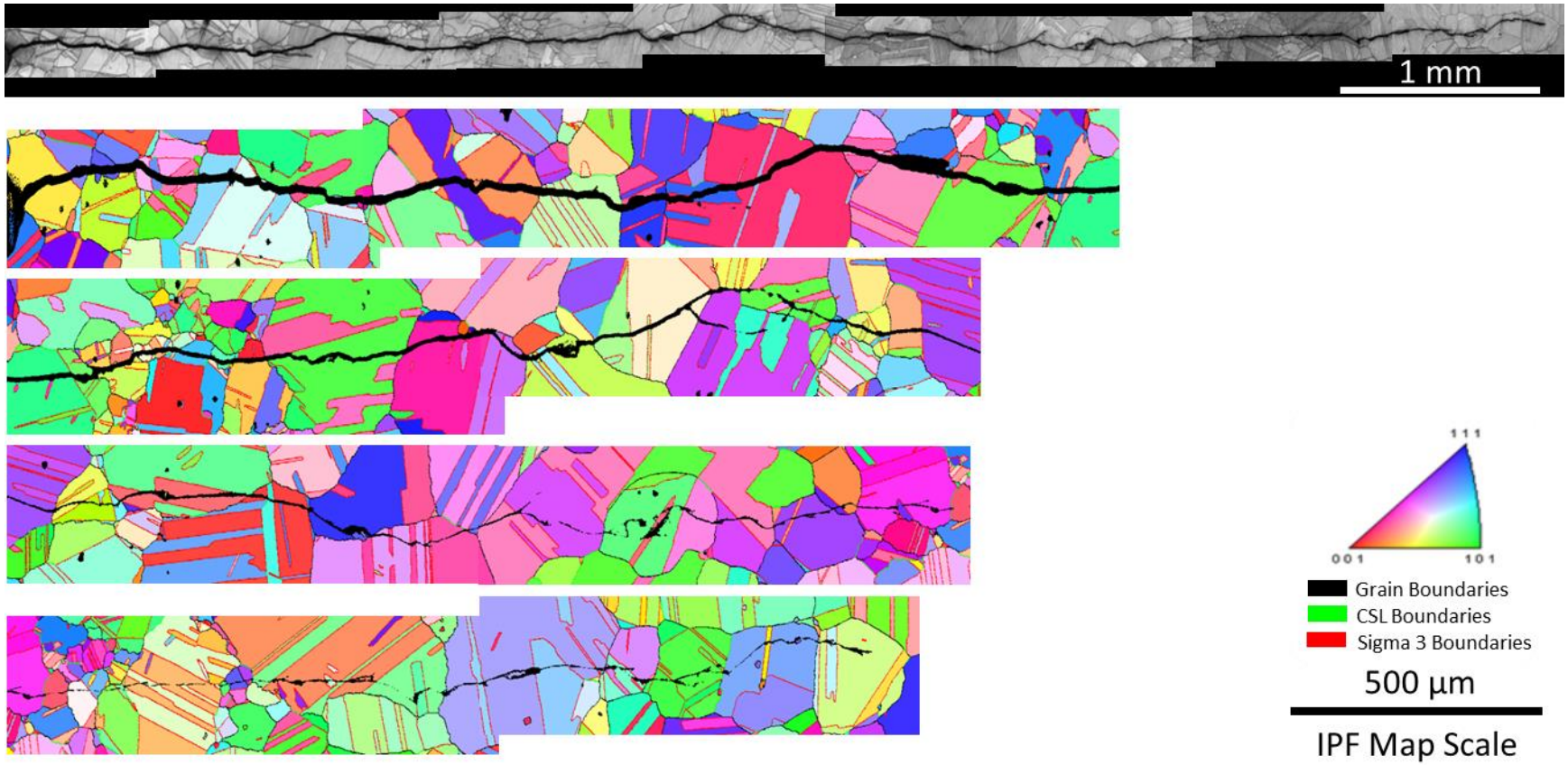


**Figure 13. EBSD results for sample: lab air, Iteration 1 (Side 1). (Top) Image quality (IQ) map of the entire crack length where the lighter pixels have a higher the image quality. (Bottom Series) IPF map where the grain orientation is represented by colors seen within the unit triangle legend and the type of boundary is indicated by color.**

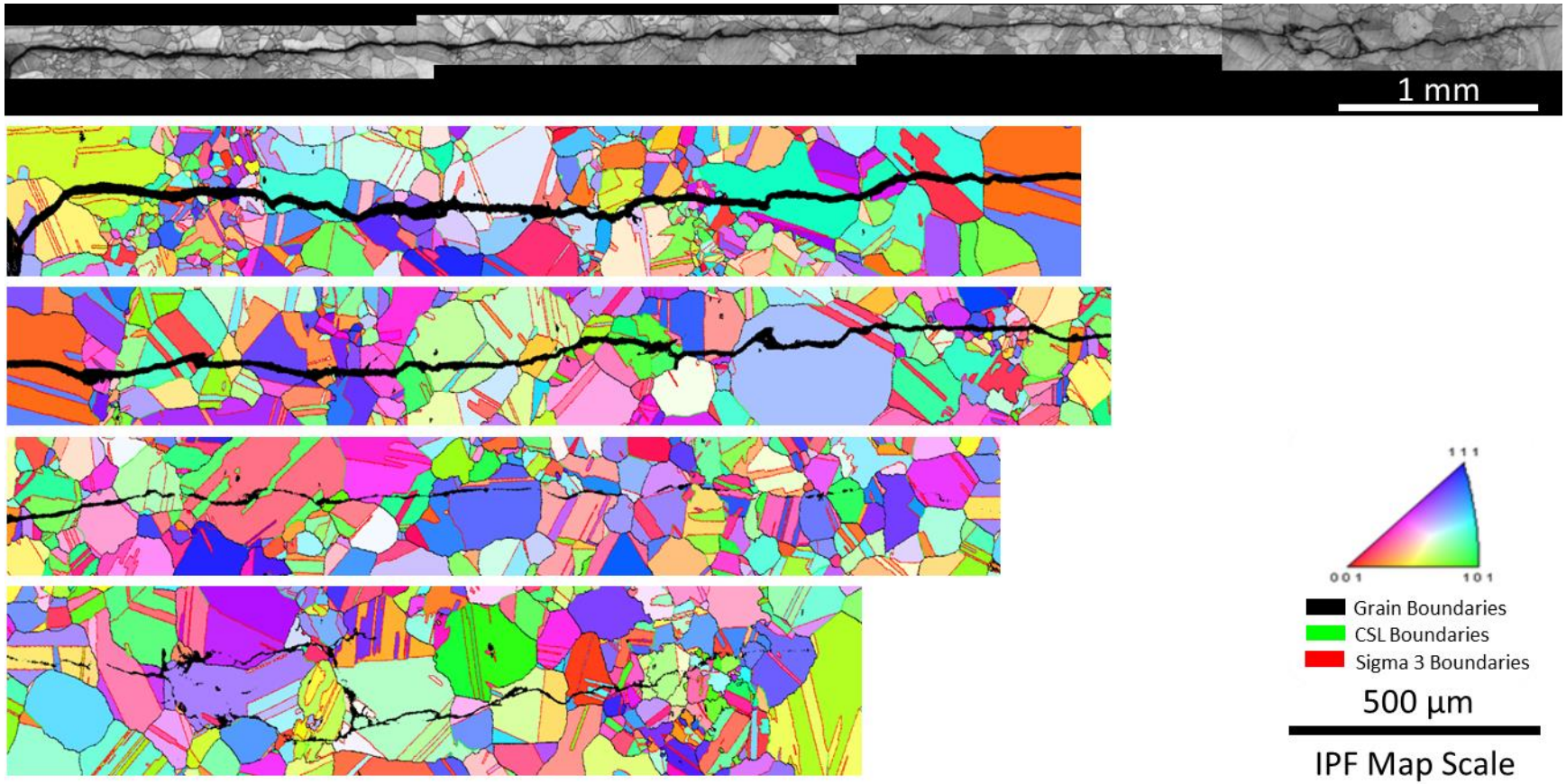


**Figure 14. EBSD results for sample: lab air, Iteration 1 (Side 2). (Top) Image quality (IQ) map of the entire crack length where the lighter pixels have a higher the image quality. (Bottom Series) IPF map where the grain orientation is represented by colors seen within the unit triangle legend and the type of boundary is indicated by color. Yellow lines are general grain boundaries, green lines are CSL boundaries and red lines are Σ3 boundaries.**

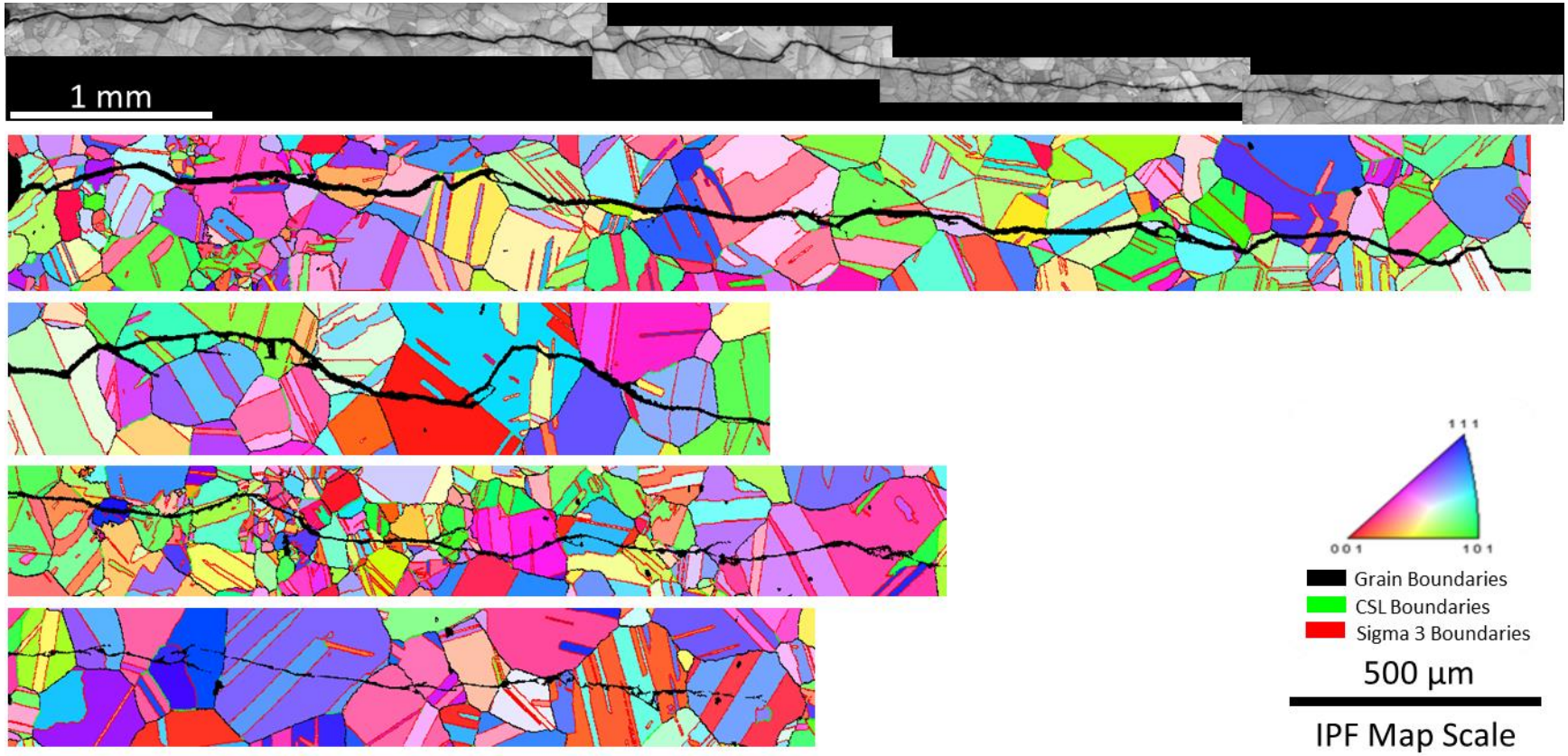


**Figure 15. EBSD results for sample: lab air, Iteration 3 (Side 1). (Top) Image quality (IQ) map of the entire crack length where the lighter pixels have a higher the image quality. (Bottom Series) IPF map where the grain orientation is represented by colors seen within the unit triangle legend and the type of boundary is indicated by color. Yellow lines are general grain boundaries, green lines are CSL boundaries and red lines are Σ3 boundaries.**

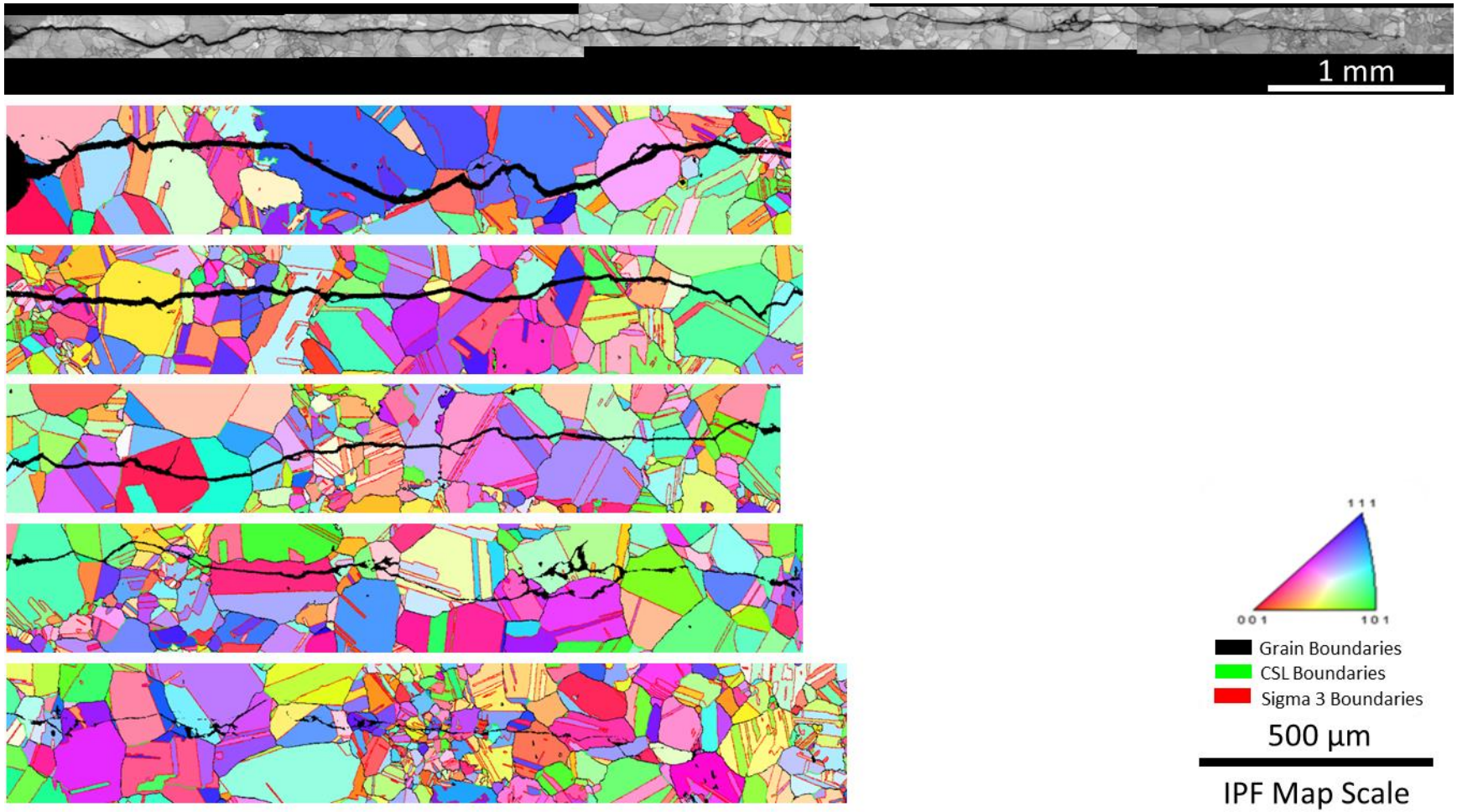


**Figure 16. EBSD results for sample: lab air, Iteration 3 (Side 2). (Top) Image quality (IQ) map of the entire crack length where the lighter pixels have a higher the image quality. (Bottom Series) IPF map where the grain orientation is represented by colors seen within the unit triangle legend and the type of boundary is indicated by color. Yellow lines are general grain boundaries, green lines are CSL boundaries and red lines are Σ3 boundaries.**

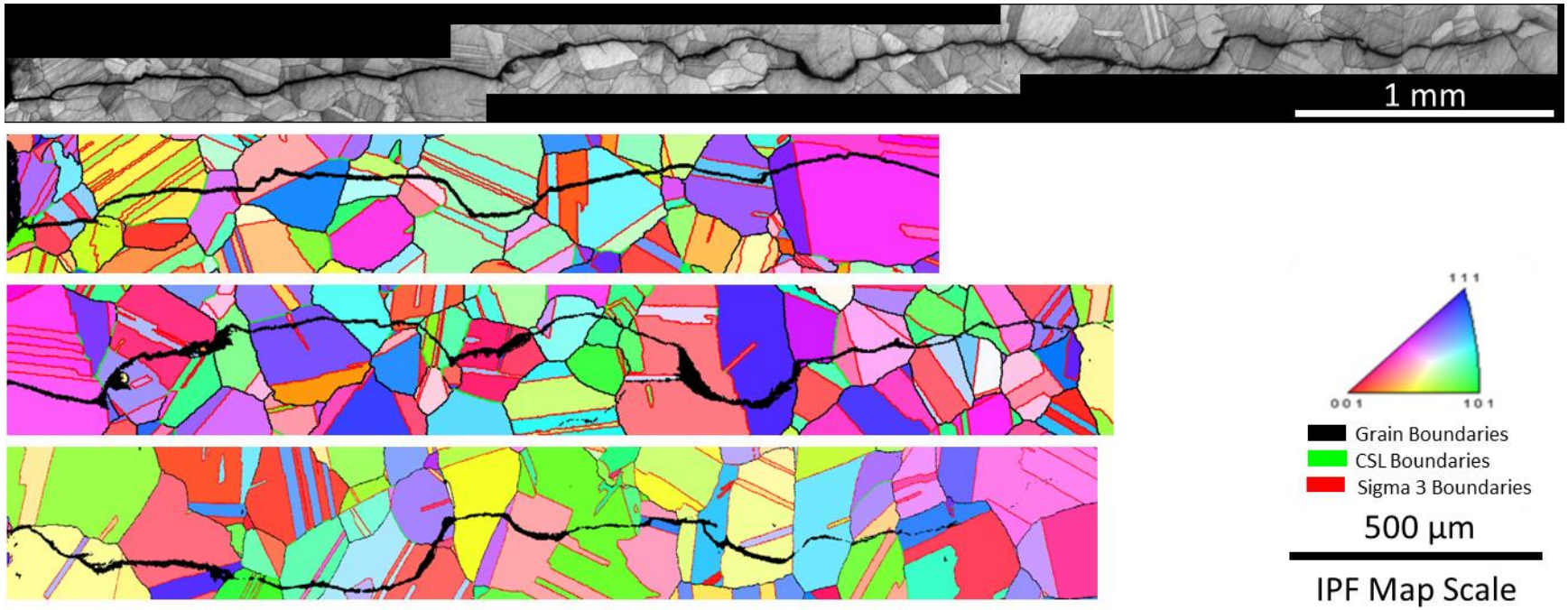


**Figure 17. EBSD results for sample: impure-helium, Iteration 1 (Side 1). (Top) Image quality (IQ) map of the entire crack length where the lighter pixels have a higher the image quality. (Bottom Series) IPF map where the grain orientation is represented by colors seen within the unit triangle legend and the type of boundary is indicated by color. Yellow lines are general grain boundaries, green lines are CSL boundaries and red lines are Σ3 boundaries.**

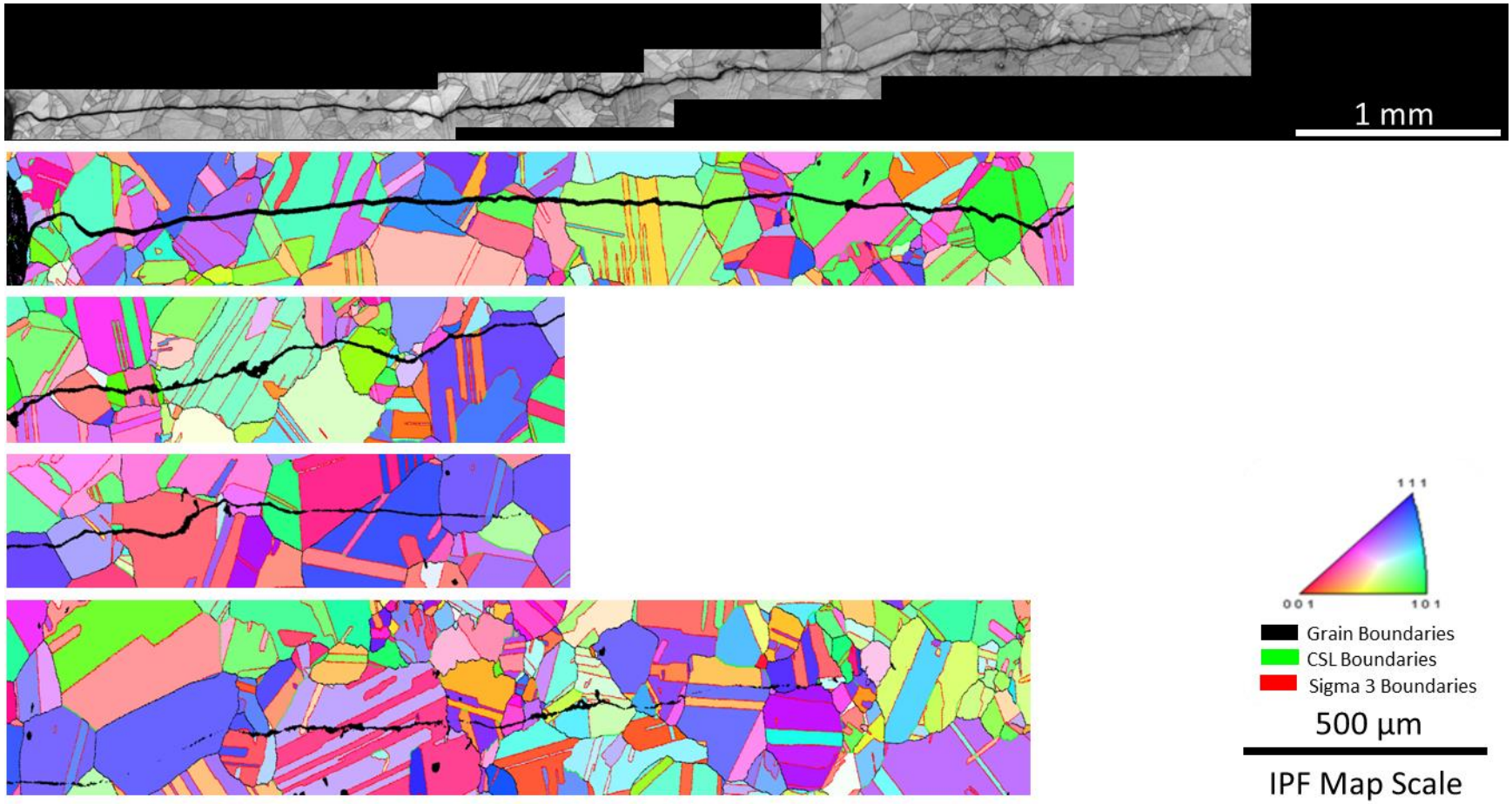


**Figure 18. EBSD results for sample: impure-helium, Iteration 1 (Side 2). (Top) Image quality (IQ) map of the entire crack length where the lighter pixels have a higher the image quality. (Bottom Series) IPF map where the grain orientation is represented by colors seen within the unit triangle legend and the type of boundary is indicated by color. Yellow lines are general grain boundaries, green lines are CSL boundaries and red lines are Σ3 boundaries.**

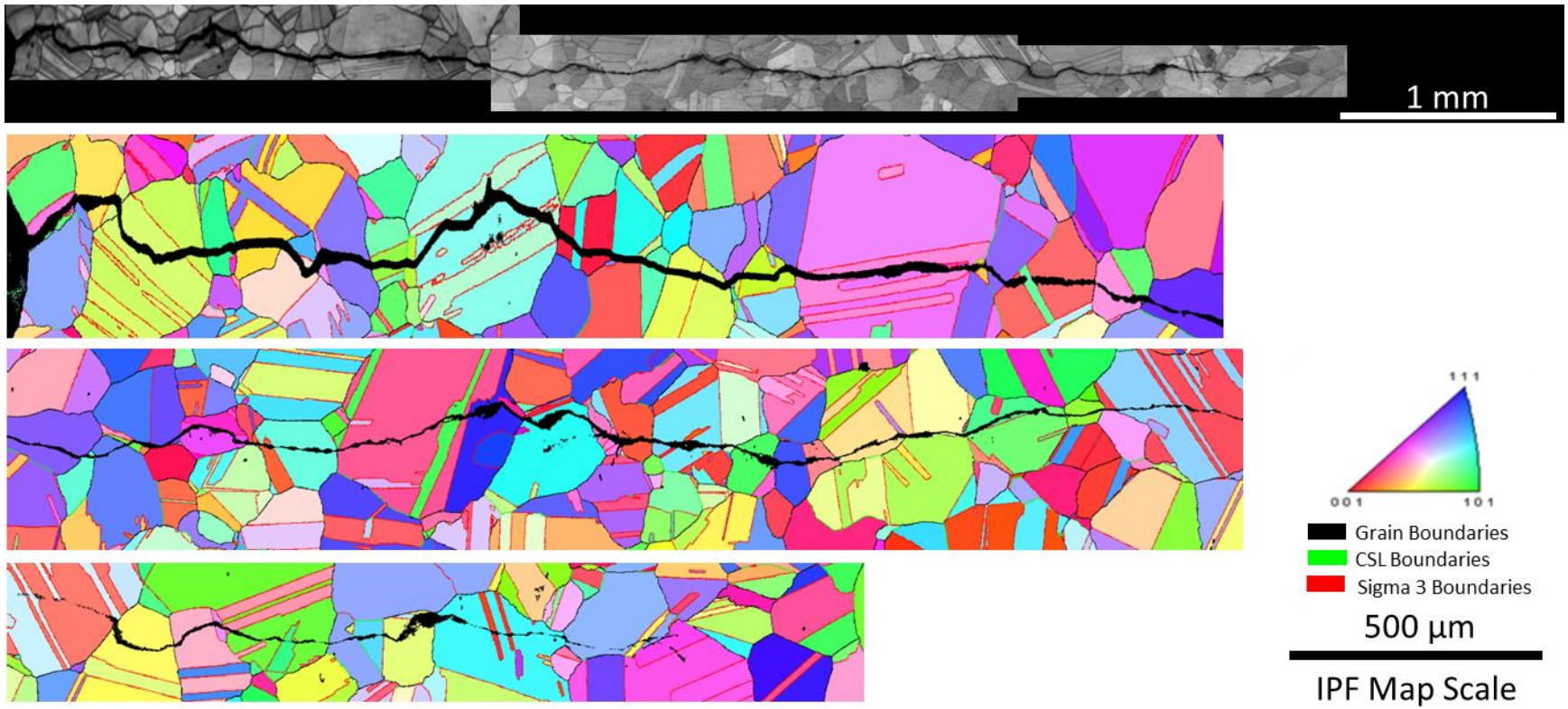


**Figure 19. EBSD results for sample: impure-helium, Iteration 2 (Side 1). (Top) Image quality (IQ) map of the entire crack length where the lighter pixels have a higher the image quality. (Bottom Series) IPF map where the grain orientation is represented by colors seen within the unit triangle legend and the type of boundary is indicated by color. Yellow lines are general grain boundaries, green lines are CSL boundaries and red lines are Σ3 boundaries.**

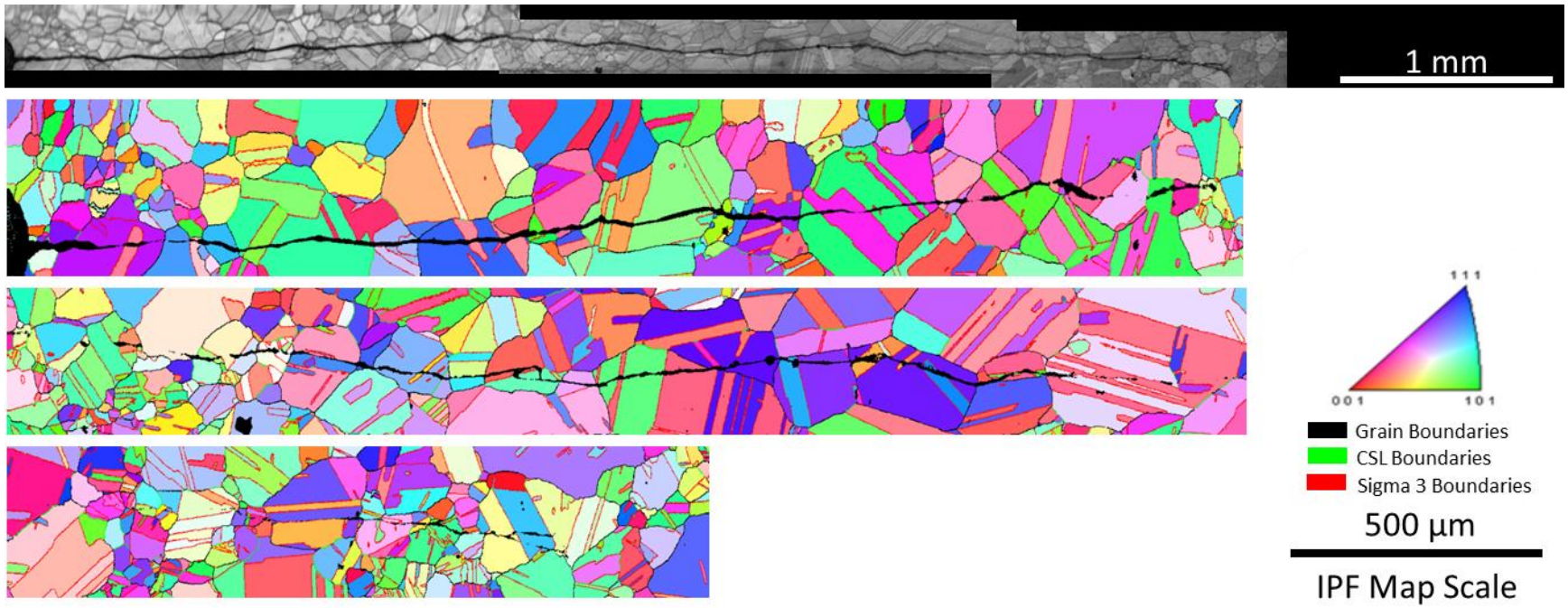


**Figure 20. EBSD results for sample: impure-helium, Iteration 2 (Side 2). (Top) Image quality (IQ) map of the entire crack length where the lighter pixels have a higher the image quality. (Bottom Series) IPF map where the grain orientation is represented by colors seen within the unit triangle legend and the type of boundary is indicated by color. Yellow lines are general grain boundaries, green lines are CSL boundaries and red lines are Σ3 boundaries.**

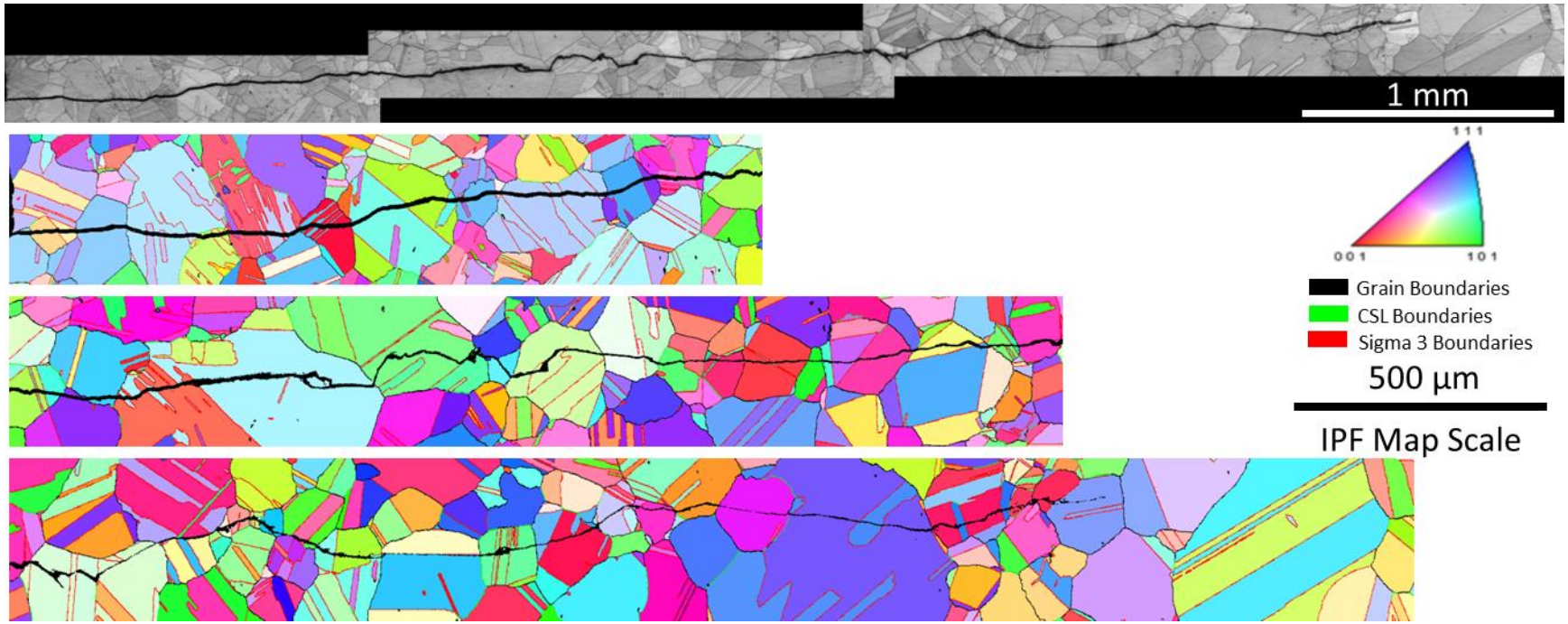


**Figure 21. EBSD results for sample: impure-helium, Iteration 3 (Side 1). (Top) Image quality (IQ) map of the entire crack length where the lighter pixels have a higher the image quality. (Bottom Series) IPF map where the grain orientation is represented by colors seen within the unit triangle legend and the type of boundary is indicated by color. Yellow lines are general grain boundaries, green lines are CSL boundaries and red lines are Σ3 boundaries.**

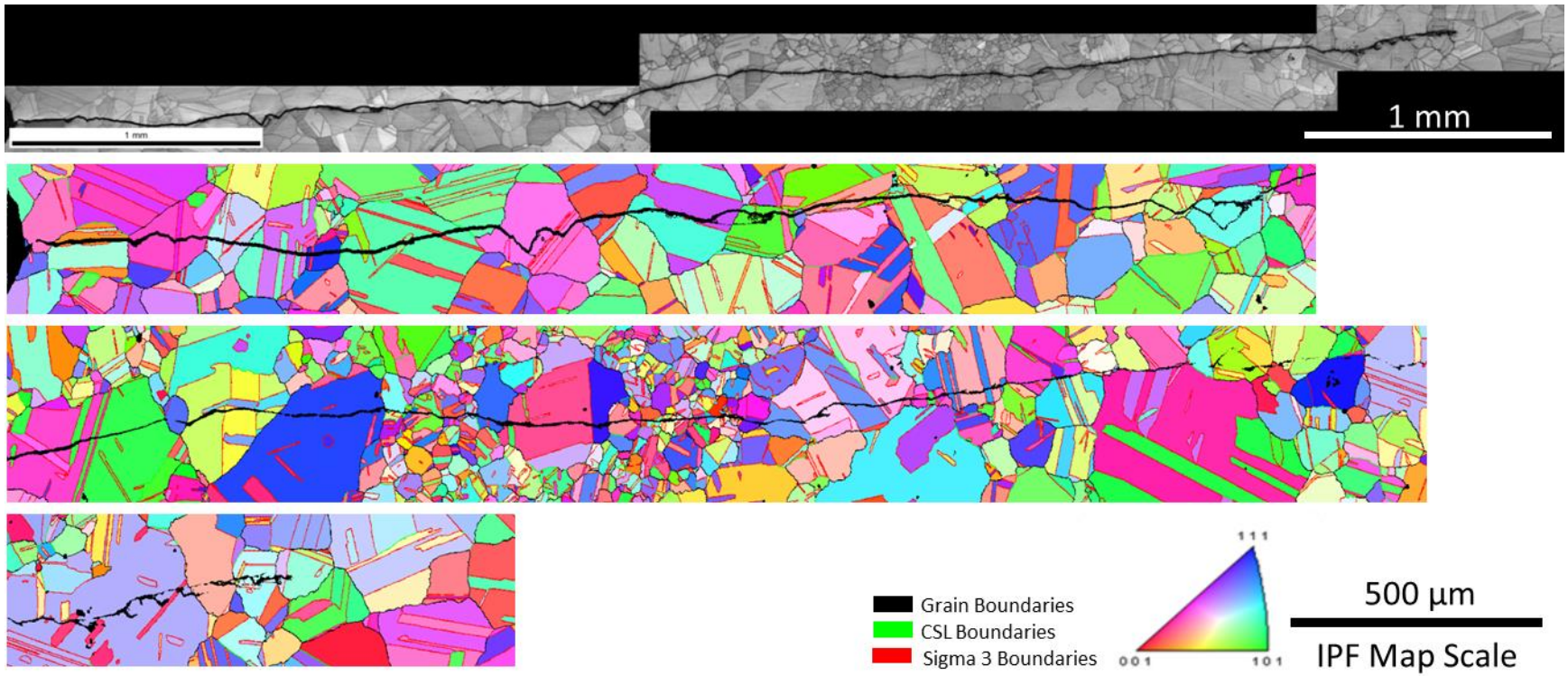


**Figure 22. EBSD results for sample: impure-helium, Iteration 3 (Side 2). (Top) Image quality (IQ) map of the entire crack length where the lighter pixels have a higher the image quality. (Bottom Series) IPF map where the grain orientation is represented by colors seen within the unit triangle legend and the type of boundary is indicated by color. Yellow lines are general grain boundaries, green lines are CSL boundaries and red lines are Σ3 boundaries.**

4.1.1: Bulk Microstructural Analysis

Electron backscatter diffraction analysis offers a means to investigate the microstructural character of a material, including the average grain size, texture, and phase distributions. Figure 23 shows the grain size distributions, with twin boundaries excluded, of the impure-helium and lab air samples. Both samples have approximately the same distribution with an average grain diameter of 80 μm.

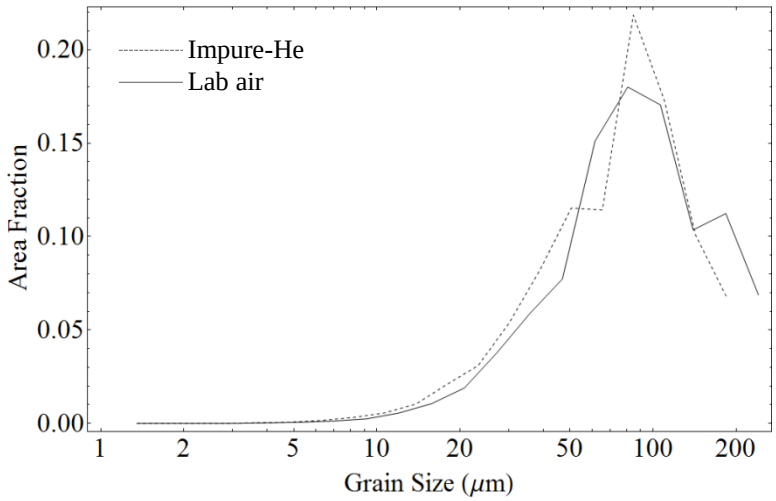


**Figure 23. Grain size distributions, with ∑3 grain boundaries excluded, of the impure-He and lab air samples.**

The texture analysis, Figure 24, of both the impure-helium and lab air samples shows a maximum texture intensity of 1.645 and 1.811, respectively. A texture intensity of 1.5 means that the texture has an intensity of 1.5 over that of a random distribution; therefore, the textures in both samples are weak.

The phase distributions of the samples illustrate that both the impure-helium and lab air samples are homogenous with little phase separation. There was a small amount of secondary phase, less than 1% of the area fraction. EDS analysis found that the secondary phase had a high concentration of titanium and EBSD subsequently indexed

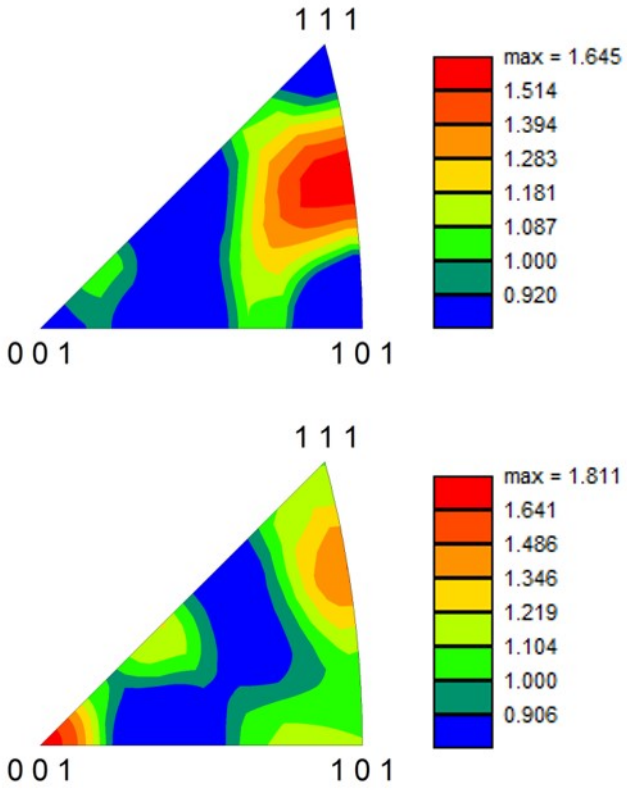


**Figure 24. Inverse pole figure unit triangles show the texture intensities for the impure-helium (top) and lab air (bottom) samples.**

the phase with high confidence as a cubic structure with the point group symmetry $m\bar{3}m$. However, the resolution of either technique does not allow for determining if the secondary phase is a titanium carbide or nitride as both have similar lattice parameters. Because of the low area fraction and slight interaction with crack propagation, the secondary phase is not considered in this study.

### 4.2: Microstructural Characterization of Crack Propagation

The first analysis performed was the direction of crack propagation through the microstructure. This data will allow insight into the effects of the experimental parameters, environment, and microstructure in determining the path of fatigue cracks.

In Figure 25, the 2D and 3D unit triangle inverse pole figure density histograms for the impure-helium sample are found. In (a) and (c), the location of each square in the figure represents the direction in the grain parallel to crack propagation; while the color and/or height represents the concentration of data points for that direction. In (b) and (d), the squares within the unit triangle represents the concentration of crack propagation planes. In these plots, blue represents a lower relative count while red is a high relative count of points representing the crack propagation directions and planes. It is seen in the figures that the crack has less propensity to propagate in the [111] direction and the most in the

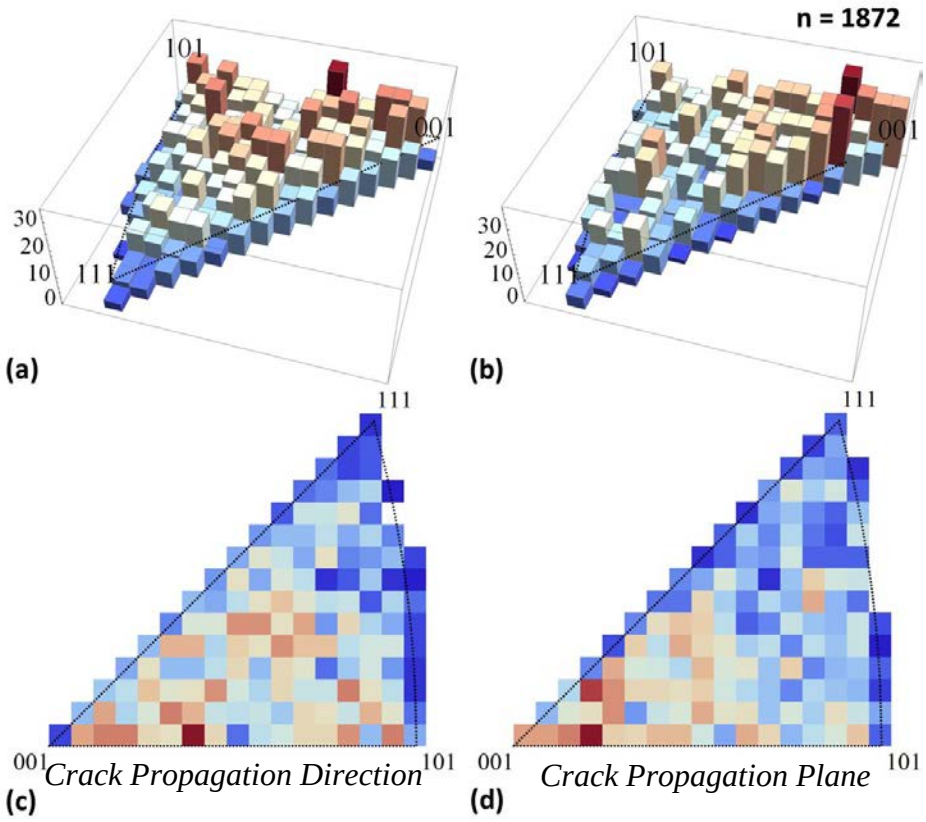


**Figure 25. Crack propagation directions and planes for the impure-He sample. (a) Three dimensional histogram showing the concentration of propagation directions (b) Three dimensional histogram showing the concentration of crack propagation planes (c) Density histogram showing the concentration of propagation directions (d) Density histogram showing the concentration of crack propagation planes**

[001] to [112] directions. It can also be seen that the (001) is the most likely crack plane. This same trend is found in the lab air sample as seen in Figure 26.

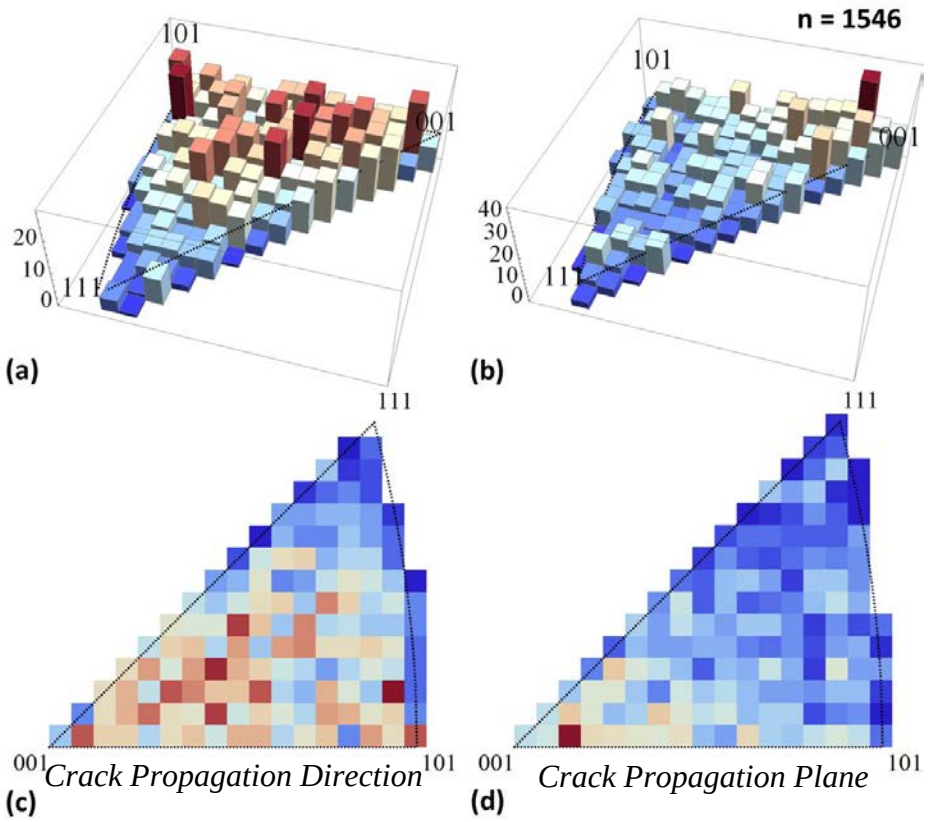


**Figure 26. Crack propagation directions and planes for the air sample. (a) Three dimensional histogram showing the concentration of propagation directions (b) Three dimensional histogram showing the concentration of crack propagation planes (c) Density histogram showing the concentration of propagation directions (d) Density histogram showing the concentration of crack propagation planes**

Similar results to that of the overall impure-helium and lab air samples were obtained when isolating testing parameters (Figure 27). In this figure each testing parameter is represented: the top row is the two waveforms (triangular and trapezoidal), the middle row is the frequencies (0.1 Hz and 0.5 Hz), and the bottom row is the three values for $K_{max}$ (20 MPa√m, 25 MPa√m, and 30 MPa√m). This is repeated for both crack direction and crack plane normal. A similar trend is seen those as in Figures 25-26, suggesting that the crack path at the microstructural level is influenced by the grain

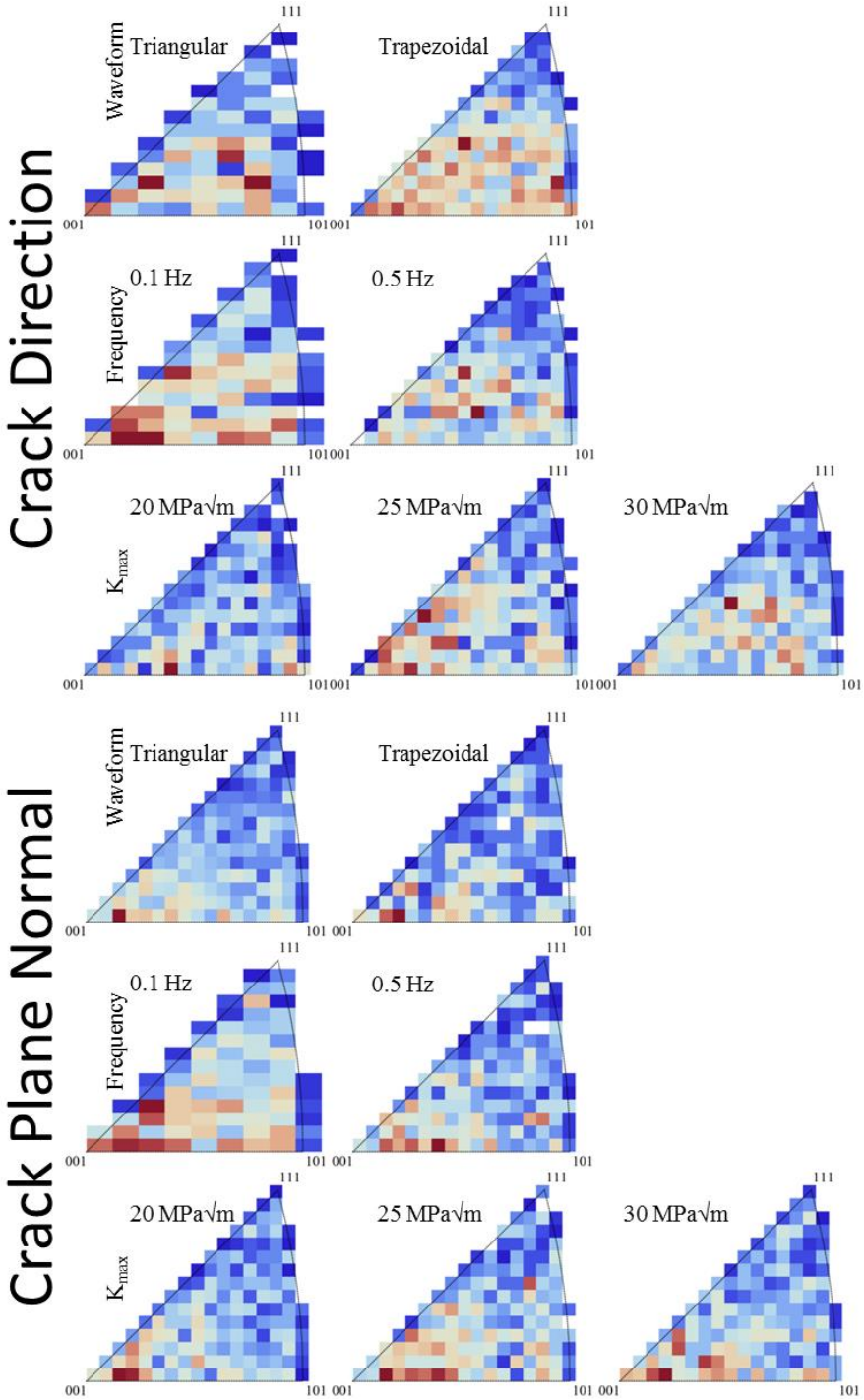


**Figure 27. The density histograms for each experimental parameter.**

orientation and not the testing environment or parameters. In order to confirm that the above results are from the interactions of the crack with the microstructure and not an

artifact of the sampling procedure, a random dataset was collected. In this sampling, measurements from random vectors taken from multiple samples were obtained. Figure 28 contains this data and it can be seen that the directions are uniformly distributed showing the previous trends are a relevant result.

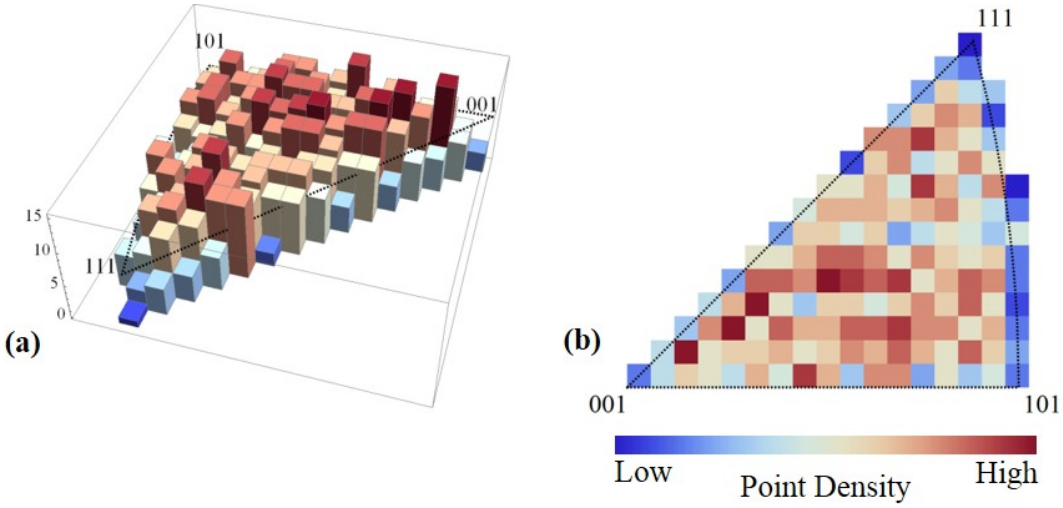


**Figure 28. Angle of crack propagation for a random sample. (a) 3D and (b) 2D density histogram showing the concentration of directions**

### 4.3: Change in Crack Propagation Direction

As the crack propagates through the sample, there are points where there is a defined change in direction (Figure 29). In this analysis, the angle of this deflection is assessed. In Figure 30, all crack deflection angles are displayed in a histogram. The most probable deflection angles are those below 20°.


**Figure 29. IPF map showing examples of well-defined crack path changes (green circles) and those with less definition (red circles). Only a small selection of crack path deviations is marked**

The next step of this analysis was to determine if where the deflection occurred carries any significance. Three location types were investigated: those that occurred at Σ3 special boundaries, at general boundaries, and within the grain. Other types of special boundaries were not included in this study due to their minimal occurrence and interaction with the crack. An analysis of variance, ANOVA, was used to determine statistical significance of each deviation location. Four location types were defined for

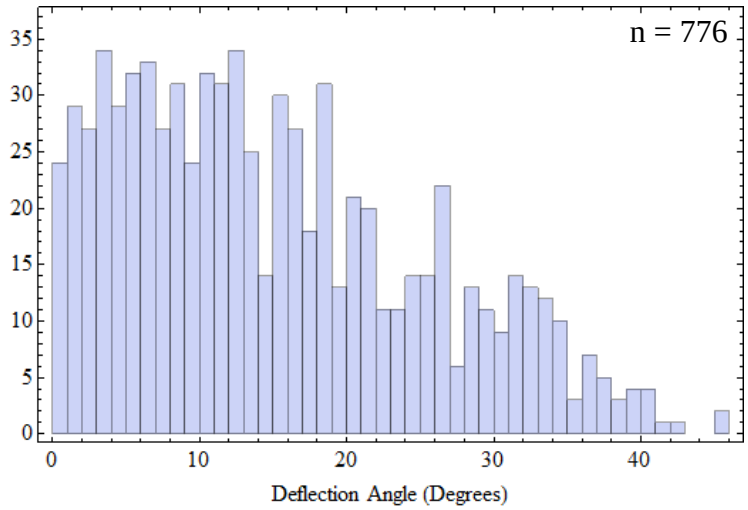


**Figure 30. Histogram of all crack propagation deflection angles for both samples.**

the statistical analysis, deviations: within the grain, at general grain boundaries, at Σ3 grain boundaries, and at all grain boundaries (Σ3 and general grain boundaries combined). Figure 31 contains histograms for each location type investigated: parts (a) through (c) are the general grain boundary, Σ3 grain boundary, and combined grain boundary deflection location types, respectively. Part (d) is the histogram for the deflections that occurred within the grains. The lines in parts (c) and (d) are the probability density functions for the datasets.

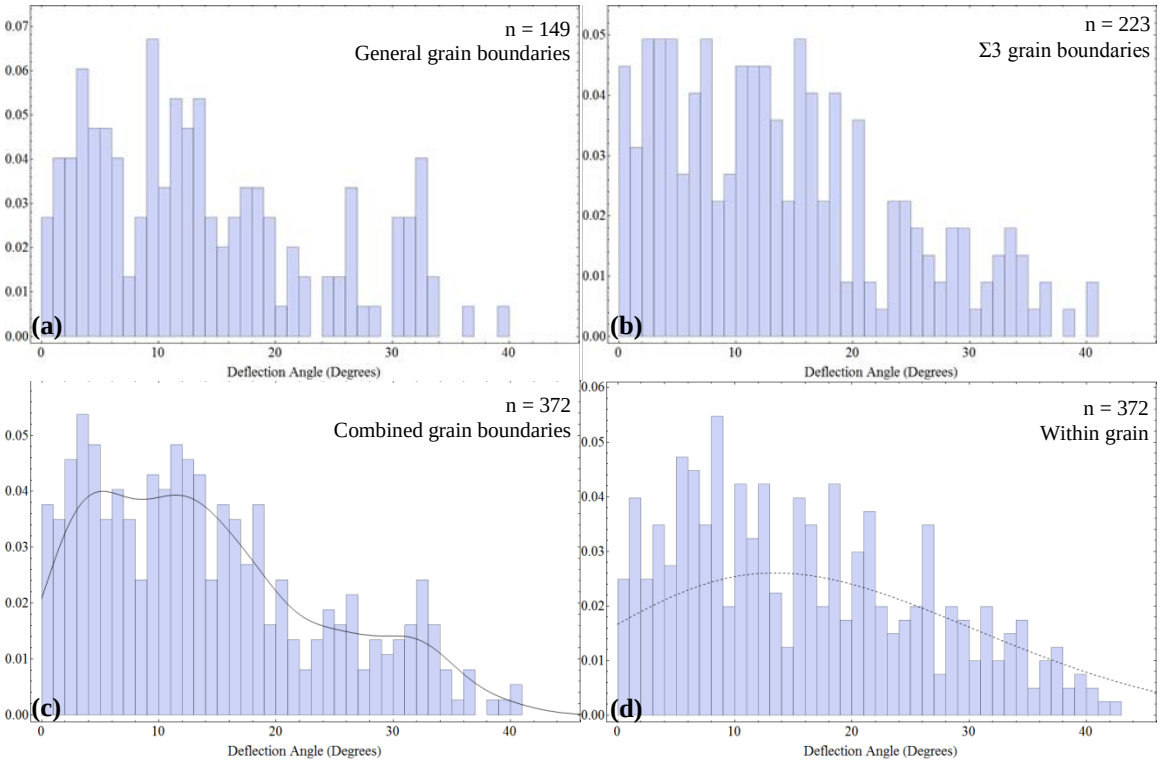


**Figure 31. Histogram of deflection angles occurring at (a) general grain boundaries (b) Σ3 grain boundaries (c) combined grain boundaries and (d) within grain. The lines in (c) and (d) are the probability density functions for the dataset.**

Performing an ANOVA with all the three unique location types (within grain, general grain boundaries, and Σ3 grain boundaries) revealed a significant difference: $F(2, 773) = 4.070$, $p = 0.017$, where a lower p-value indicates a greater significance. It is customary to consider $p = 0.05$ or $0.01$ as the cutoff, depending on the level of

significance needed to be achieved [87, 88]. In order to determine which of the location types were significant in the ANOVA, a post-test was needed. Tukey's honestly significant difference test [87] determined that at a significance level of 0.05 the deviations within the grain verses at the Σ3 grain boundaries are significant. In other words, the deflections seen at Σ3 grain boundaries are statically different from those that occur within grains. At a significance of 0.1, the deviations within grain verses general grain boundaries are also determined significant, however, this is not high enough significance to consider relevant.

In the next ANOVA, the general grain boundaries and Σ3 grain boundaries are analyzed without the data for within the grain. It was found that there are no statistically significant differences as determined by one-way ANOVA ($F( 1, 370 ) = 0.007$ , $p = 0.932$). In other words, the deflection at grain boundaries is not statistically affected by the character of the grain boundary. With those results, the data for both types of grain boundaries were combined.

By comparing the within grain deviations to those at the combined grain boundaries, the highest level of significance was obtained: $F(1, 775) = 8.143$, $p = 0.004$. Therefore it was determined that there was significant differences between the deviations at the combined grain boundaries verses the deviations within the grain. The histogram in Figure 31(d) shows that the within grain deviations are unimodal with a mean of 16° and a standard deviation of 15° suggesting no significant difference for deviation angles between 0-30°. The combined grain boundary dataset, Figure 31(c), shows a multi-modal distribution suggesting up to three possible mechanisms for crack deviation.

The ANOVA results for the condition combinations are summarized in Table 5. In this table, both the location within the microstructure and test parameters are included in the first two columns. The third column is the F-ratio, which can be thought of a measure of how different the means are relative to the variability within each location type [88]. Larger F-ratios have greater likelihood that the differences are due to something other than chance alone [87]. The fourth column is significance level determined by the ANOVA. The results of the post-test are contained in the last column. This shows which parameters or location types were found to be significant. There is not any statistical significance for the following test parameters: waveform, frequency, $K_{max}$, and environment; therefore, these parameters are not responsible for the deflection angles.

**Table 5. The analysis of variance, ANOVA, results for the testing parameters, environment and deviation location**

| ***Parameter*** | ***Conditions*** | ***F-ratio*** | ***Sig. Level*** | ***Sig.[1]*** |
|---|---|---|---|---|
| *Waveform[2]* | Tri, Trap | $F(1, 485) = 3.048$ | $p = 0.08$ | n.s. |
| *Frequency[3]* | 0.01, 0.05 | $F(1, 357) = 0.796$ | $p = 0.37$ | n.s. |
| $K_{max}$[4] | 20, 25, 30 | $F(2,729) = 1.930$ | $p = 0.15$ | n.s. |
| *Environment* | Im-He, Air | $F(1, 385) = 0.463$ | $p = 0.50$ | n.s. |
| *Location[5]* | GB, Σ3, IG, AllGB | $F(3, 1144) = 3.770$ | $p = 0.010$ | IG, AllGB<br>IG, Σ3[5] |
| | GB, Σ3, IG | $F(2, 773) = 4.070$ | $p = 0.017$ | IG, Σ3<br>IG, GB[5] |
| | IG, AllGB | $F(1, 774) = 8.143$ | $p = 0.004$ | IG, AllGB |

*[1]n.s. = not significant; [2]"tri" = Triangular, "Trap" = Trapezoidal; [3]Hz [4]MPa√m; [5]"GB" = General Boundary, "Σ3" = Sigma 3 boundary, "IG" = Within Grain, "AllGB" = All grain boundaries [5]0.05 < p < 0.10*

### 4.4: Areas of Recrystallization

In this study, evidence of recrystallization during fatigue crack growth was found. Figure 32 shows one such area, located within the impure-He sample with the following parameters: $K_{max}$ of 30 MPa√m, triangular waveform, and 0.05 Hz loading frequency. The crack propagation path in this figure is from the bottom to the top. The image on the

left is IPF map of the area in question. A number of small 1-5 μm grains are seen on both sides of the fatigue crack in the area of the sharp deviation. The small grains are only seen in this area and not within the bulk of the material. The deviations occur relatively close to Σ3 grain boundaries and between the deviations, the crack propagates close to but not along a general boundary. The image on the right is the local misorientation map of the same area. The areas away from the crack and those within the small grains show a misorientation of 0-1°, while outside of the small grain area, misorientation of approximately 1-4° can be found. This finding suggests that the small grains have little to no residual strain as might be expected from the passing of the plastic zone ahead of the crack tip, though the area just outside of the small grain area shows the expected residual strain. A second area of recrystallization can be seen in Figure 33. This is also located within the impure-He sample with the following parameters: $K_{max}$ of 30 MPa√m,

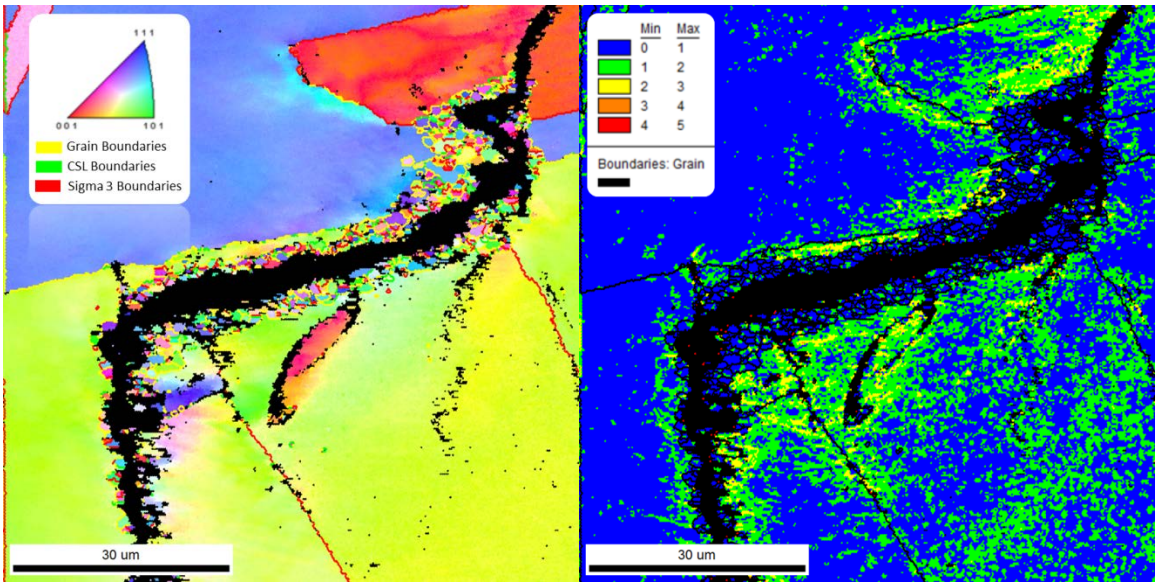


**Figure 32. Recrystallization area 1 located in the impure-He sample with a $K_{max}$ of 30 MPa√m, triangular waveform, 0.5 r-ratio and 0.05 Hz loading frequency. (Left) IPF map of area of recrystallization. The grain boundary type is represented as (yellow) general, (green) special CSL, and (red) Σ3 boundaries. (Right) Local misorientation map with blue representing 0-1° and red representing 4-5° of misorientation. Grain boundaries are shown as black lines. Black areas in both maps represent the crack and other areas of low image quality.**

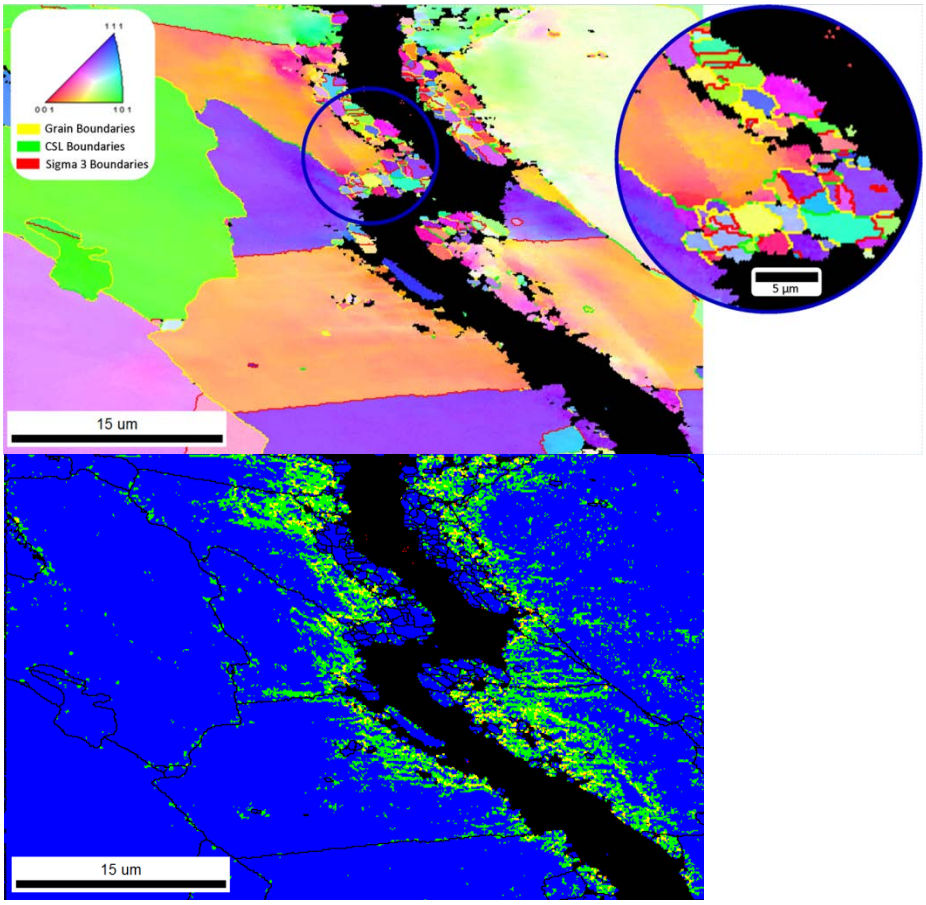


**Figure 33. Recrystallization area 2 located in the impure-He sample with a $K_{max}$ of 30 MPa√m, triangular waveform, 0.5 r-ratio and 0.05 Hz loading frequency. (Left) IPF map of area of recrystallization. The grain boundary type is represented as (yellow) general, (green) special CSL, and (red) Σ3 boundaries. (Right) Local misorientation map with blue representing 0-1° and red representing 4-5° of misorientation. Grain boundaries are shown as black lines. Black areas in both maps represent the crack and other areas of low image quality.**

triangular waveform, and 0.05 Hz loading frequency. Similar trends as seen in the first recrystallization area are present such as the presence of sharp crack deviations that occur close to grain boundaries and that it propagates close to a general grain boundary. The EBSD data for both Figures 32 and 33 were taken at a step size of 0.10 µm. Due to machine time constraints, further EBSD data was taken at 0.80 µm steps. Additional areas of possible recrystallization were identified but because of the coarseness of the

data collection as compared to the grain size, they were harder to recognize. Figure 34 contains two more identified areas. Both of these were also found in the impure-He sample. The top area has the following parameters: $K_{max}$ of 25 MPa√m, triangular waveform, and 0.1 Hz loading frequency. While bottom the area in Figure 34 has these parameters: $K_{max}$ of 30 MPa√m, triangular waveform, and 0.1 Hz loading frequency.

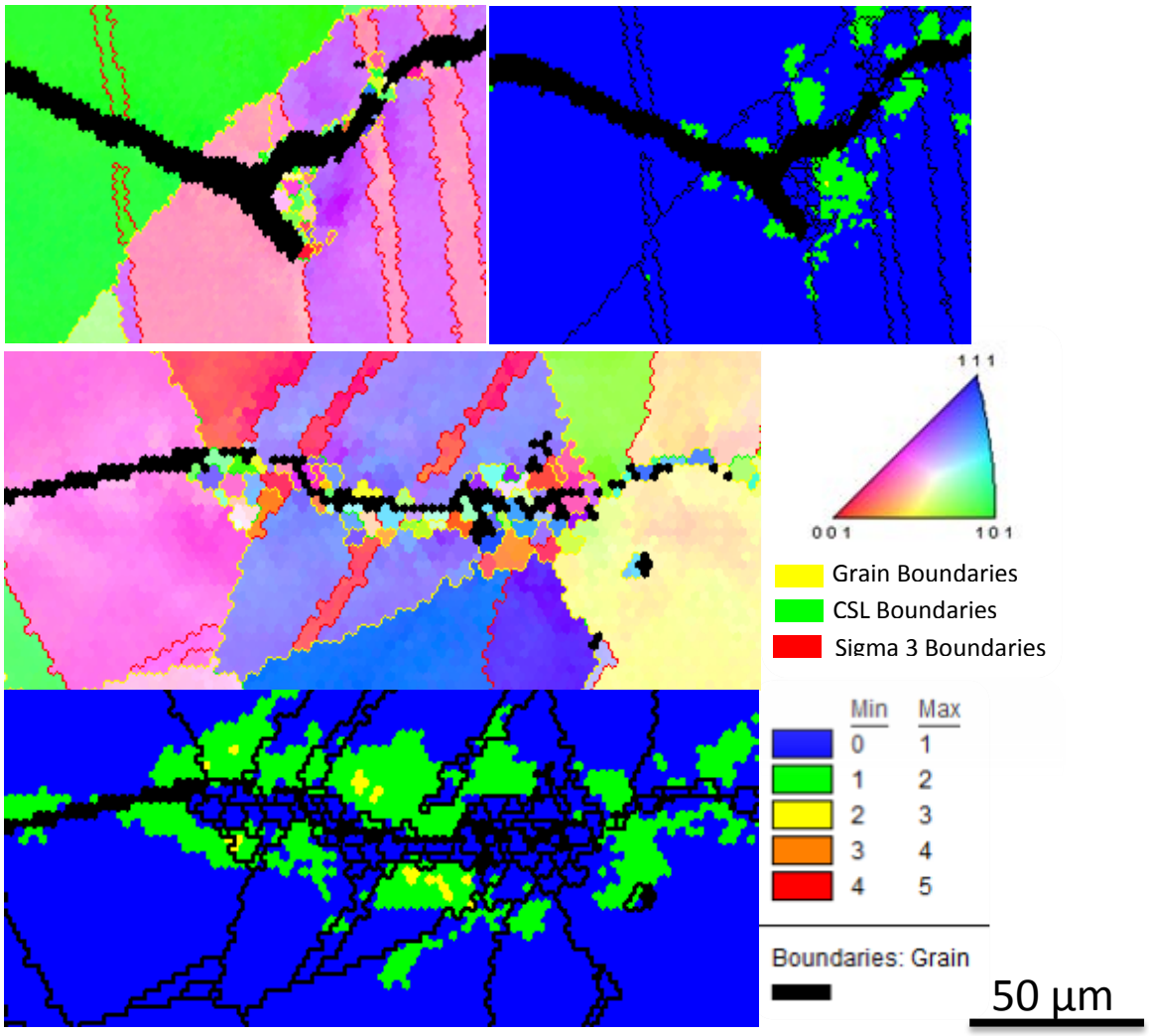


**Figure 34. Recrystallization areas 3 (top) & 4 (middle and bottom) located in the impure-He sample. Area 3 has a $K_{max}$ of 25 MPa√m, triangular waveform, and 0.1 Hz loading frequency. Area 4 has a $K_{max}$ of 30 MPa√m, triangular waveform, and 0.1 Hz loading frequency.**

# CHAPTER FIVE: DISCUSSION

## 5.1: Microstructural Influence in Fatigue Crack Propagation Direction

It can be seen in Figure 35 that the fatigue cracks produced for this work mostly follow Mode I (perpendicular to the loading axis) propagation behavior. For the first few cycles of the test, the crack behaves in Mode II (45° to the loading axis) for less than a grain width. Even those cracks that seem to start in Mode I (see the inset of Figure 35) propagate in Mode II at least for a few microns. The short Mode II section of crack propagation is expected based on the compact tension sample geometry and configuration. The machined notch simulates a crack, allowing for sample geometry where the plastic zone ahead of the crack is negligibly small compared to the crack length. In the samples used in this work, the machined crack length was 10.16 mm long, which is considered a long crack.

After the short duration of Mode II crack propagation, the overall macroscopic character of the crack is Mode I. In the impure-He sample iteration 1 (Figure 35), which is closer to the sample surface, more deviations from the plane of highest stress are seen compared to other iterations obtained deeper within the sample. This trend is not apparent in the lab air sample as both iterations show similar character. Both samples do show that there is some deviation from the plane of highest stress as the crack propagates through the sample as can be expected as the crack encounters obstacles and interacts with the microstructure.

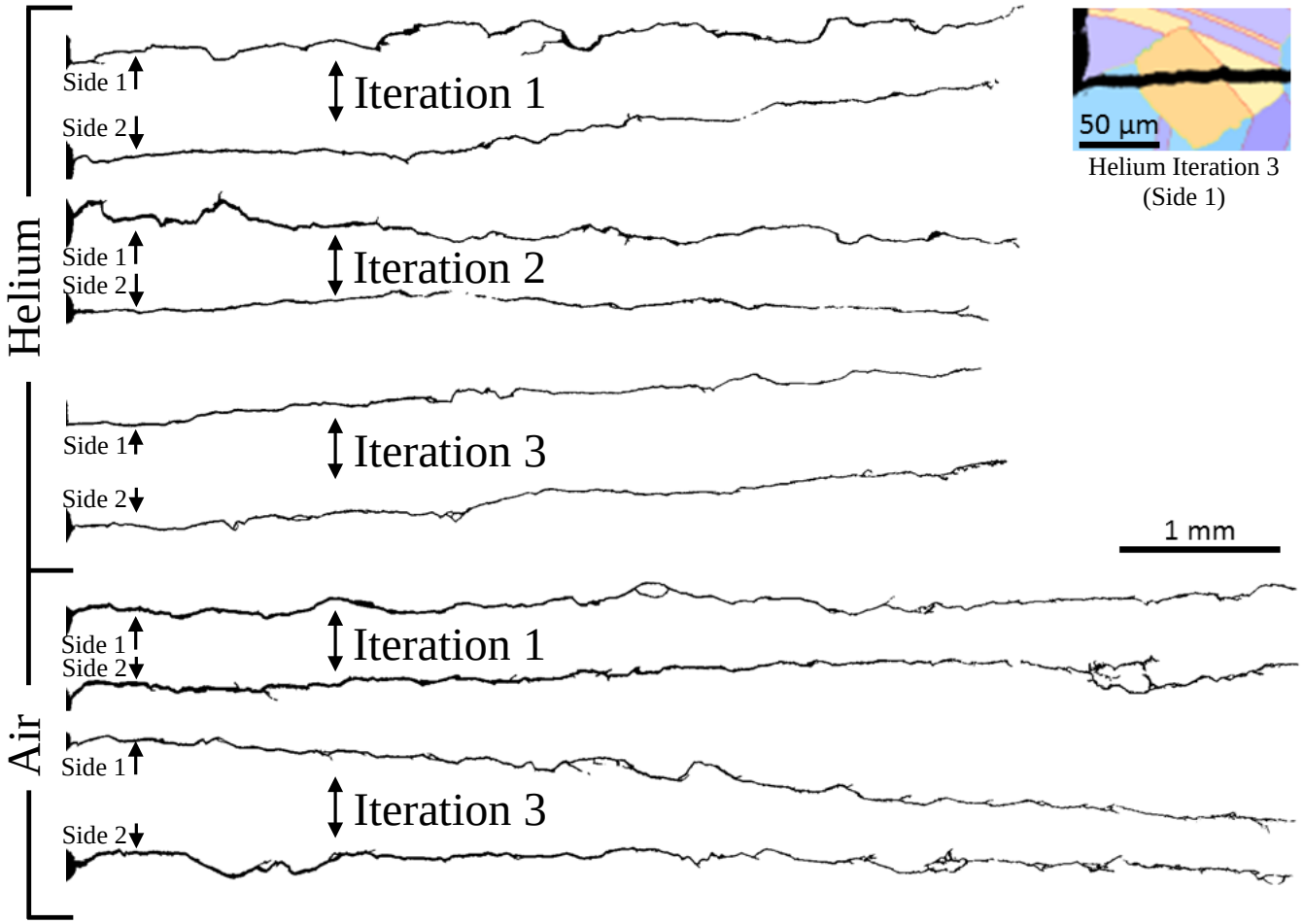


**Figure 35. Above are images showing each analyzed crack path. The inset in the upper right corner shows that at magnification crack propagation starts in mode II for the first few microns.**

5.1.1: The Modulus Effect

Figure 36 is a histogram of crack propagation directions with the color representing the relative number of times that direction occurred within the sampling, a

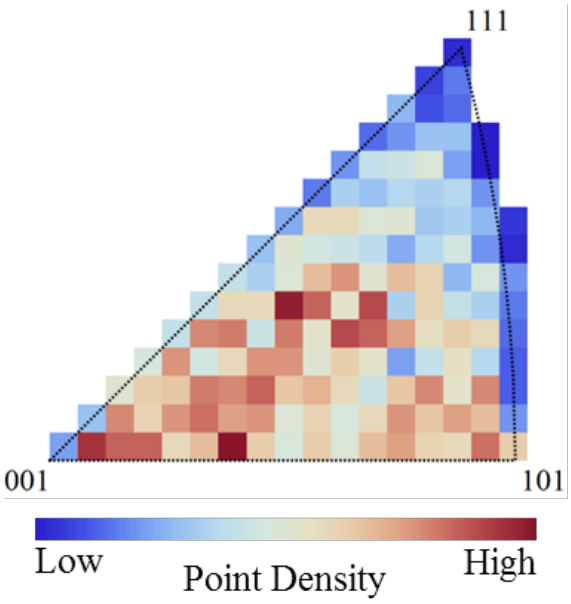


**Figure 36. Density histogram of all crack propagation directions from both samples.**

low density of points is represented by blue with higher densities being red. This shows that the crack has less propensity to propagate within the <111> family of directions and has the highest likelihood of propagating in the <100> to <112> family of directions. This trend can be related to properties of the face centered cubic structure of the material. In cubic materials, properties in a single crystal are anisotropic. For example, the elastic modulus for pure nickel is as follows: $E_{iso}$ = 207 GPa, $E_{<100>}$ = 137 GPa and $E_{<111>}$ = 305 GPa [12]. In Figure 37, the crack propagation direction density histogram is seen with the anisotropic elastic modulus of pure nickel overlaid. The results in the top of Figure 37 show that there is a correlation between the compliance of the material in a specific direction and the propensity of a fatigue crack to propagate in that direction.

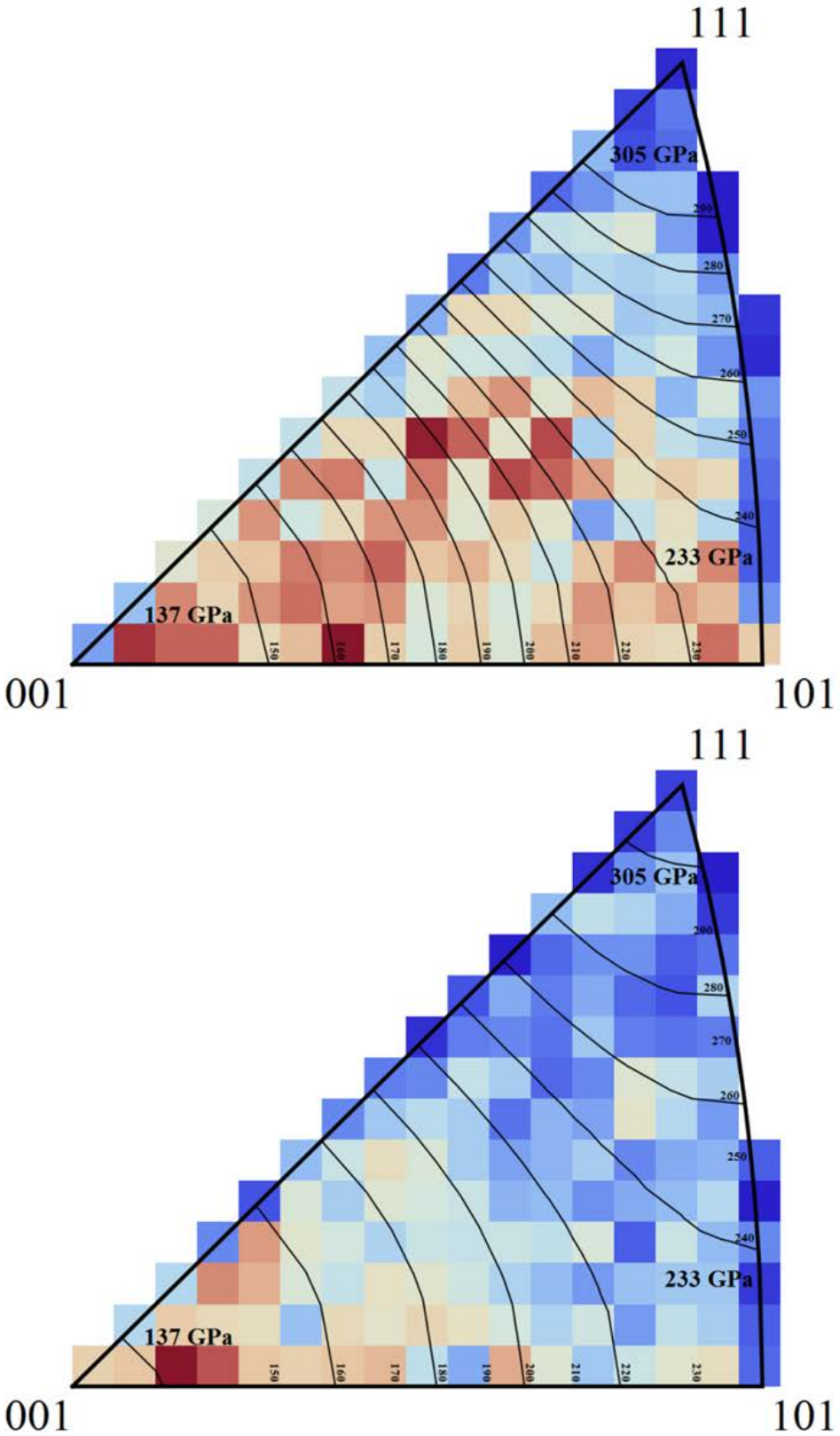


**Figure 37. Density histogram of all data points collected from crack path direction determination via EBSD with the anisotropic Young's modulus contours of nickel overlaid. (Top) Crack propagation direction (Bottom) Crack propagation plane**

Past research has shown that the elastic modulus has shown control over fatigue crack growth [89, 90]. Speidel *et al* [89] found that in a vacuum, when ΔK is normalized by the modulus, several materials show similar crack growth rates. This has been further expanded by Shahinian *et al* [90], who found the variation of the elastic modulus with temperature correlates to the variation of the crack growth rate in Alloy 718 and Type 306 stainless steel with temperature in a vacuum.

5.1.2: Quasi-Cleavage

Mode I growth is stated as essentially non-crystallographic and occurs close to the plane of maximum stress. However, the current study suggests that though on the macroscopic scale this is not true, on the microscopic scale, microstructure influences fatigue crack propagation. The traditional mechanism for microstructural influence has been studied in crack propagation, as discussed previously, the growth is predominantly on slip planes, {111} family of planes, in shear mode. However, past studies [90-92] have suggested a second mode of crack growth. Several terms have been used to distinguish this mode: faceted mode, cleavage mode, and quasi-cleavage mode [90]. This mode has been found to be active in materials that have a high degree of symmetry of the slip systems in respect to the crack plane and those that have a low stacking fault energy, such as nickel superalloys [90, 92]. In materials showing the quasi-cleavage mechanism, fatigue crack growth occurs along the {100} family of 'cleavage' planes, rather than the {111} family of slip planes. This mechanism has been observed in single crystal nickel-based superalloys such as Udimet 700 [90, 92], aluminum alloys [92], and the basal planes of titanium alloys [93]. Henderson *et al.* found that Mode I cracks in Udimet 700 had growth rates that were greatest on the {001} family of planes and least in {111}

family of planes [94]. His work also found that the cracks that propagated in the {111} family of planes showed striations with suggest the ductile slip system crack growth mechanism; while growth in {001} had flat fracture surfaces similar to cleavage surfaces.

With the quasi-cleavage mechanism of cracking, two intersecting (111) slip planes that pass through the crack front contain a common [011] slip direction correctly positioned for crack tip shear. During the crack growth cycle, the activation of the two slip systems combine and a net displacement in the [112] direction occurs [94]. The bottom image of Figure 37 is an inverse pole figure containing the measured crack propagation planes. This shows, for all data points collected, there is a strong concentration of cracking along the {001} family of planes. In Figure 38, a histogram of the crack propagation angle from the ⟨112⟩ family of directions, which shows that the average propagation angle is 14° ±18° outside of the ⟨112⟩ family of directions. An

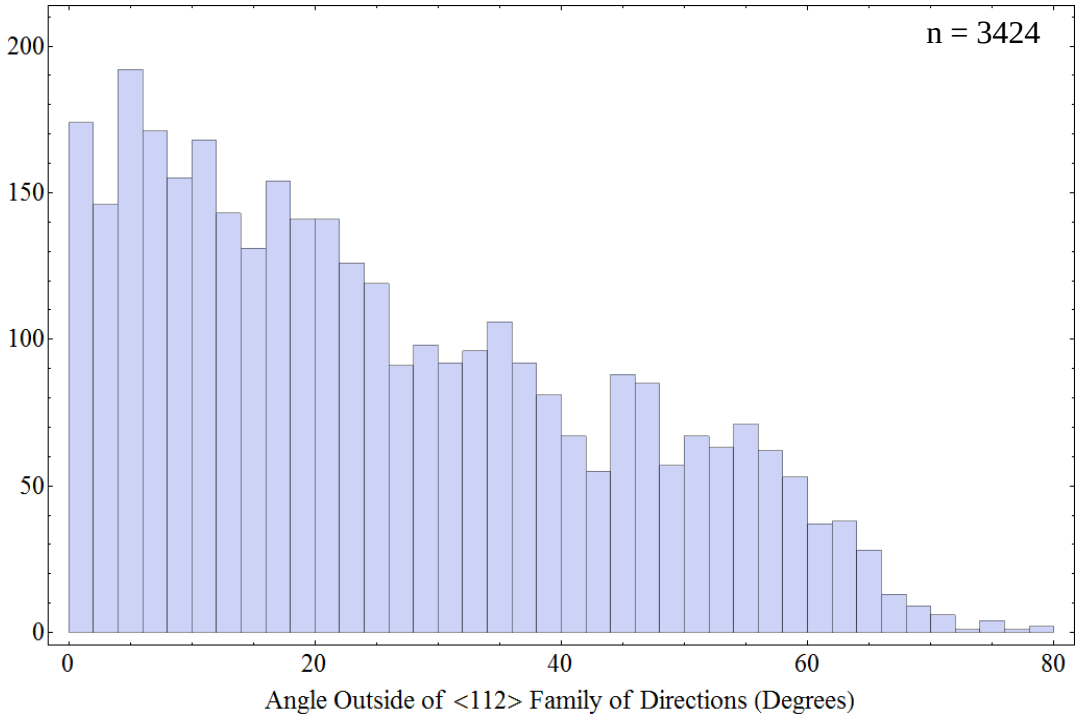


**Figure 38. Crack propagation angle away from the <112> family of directions for all samples.**

influencing factor in the propagation direction is the grooves in the side of the sample, which help contain the crack within the plane of maximum normal force. This can explain the large variation found in the crack growth direction. The crack growth data above supports the quasi-cleavage is the mechanism of crack propagation for Inconel 617 at 650 °C for the test parameters evaluated.

### 5.2: Microstructural Influence in Fatigue Crack Deflection

Another aspect of crack propagation is the deflection angle from one crack path to another. It was found that the propagation angle change found within a grain versus that at a grain boundary is statistically significant. The type of grain boundary involved, $\Sigma 3$ or general boundary, had lower significance than that there was simply a grain boundary present. Therefore, this investigation is limited to combined boundaries. Figure 31 contains the results of the deflection angle found within the grain, Figure 31(d), and at the grain boundaries, Figure 31(c). The distribution of deflection angles within the grain are unimodal with a mean at 16° ±15°. This shows that within a grain the most likely deviation angle change is below 30°. The multimodal distribution of the crack deflection angle at grain boundaries suggests that multiple mechanisms may be influencing the crack propagation direction. Because of the mixed distribution, the mean and standard deviation have little significance. The probability density function, Figure 31(c), shows that the angles with the highest probability are at 5°, 12°, and 30°.

Possible mechanisms for crack propagation deflection are encounters with secondary phases, inclusions, defects, and dislocation pileup [26, 34, 44, 95]. Microstructural characterization through EBSD confirmed that all samples were solution treated Inconel 617 with a minimal amount of secondary phases. A likely possible

mechanism for crack propagation deflection near or at a grain boundary and within the grain can be attributed to dislocation pileup [26, 44]. As the crack progresses through the grain, dislocations move ahead of the stress field generated by the crack tip [26]. When dislocations encounter the grain boundary or other obstruction, they become immobile. Therefore, the dislocation density increases ahead of the crack tip as it advances. The increased dislocation density hinders further dislocation movement within the slip system. This hardening effect allows for slip systems with a lower Schmid value to then activate. Subsequently, dislocation pile ups will influence the direction of crack propagation. For deviation at the grain boundaries, the crack propagation deviation angle can influence orientation change from one grain to another. When the crack passes into the new grain, it will propagate according to the factors dependent on orientation such as the preferred slip systems and anisotropic material properties. Therefore, the crack will change its propagation angle based on the microstructural influences.

### 5.3: Factors That Influence Fatigue Crack Propagation in Inconel 617

Figure 39 shows results from the study performed at the Idaho National Laboratory by Julian Benz from which the samples for this study were obtained. The influence of the environment and experimental parameters were not found to have a significant influence on the fatigue crack path, however, Figure 39 shows that the crack growth rate is influenced. It can be seen that the lab air sample has a higher crack growth rate than that of the impure-He sample. The largest influence on the crack growth rate is that of $K_{max}$; the higher the $K_{max}$, the higher the crack growth rate. Finally, the frequency of loading was seen to have little effect. The results in Figure 39 are in contrast to those found in this work, Table 6, which shows no statistically significant

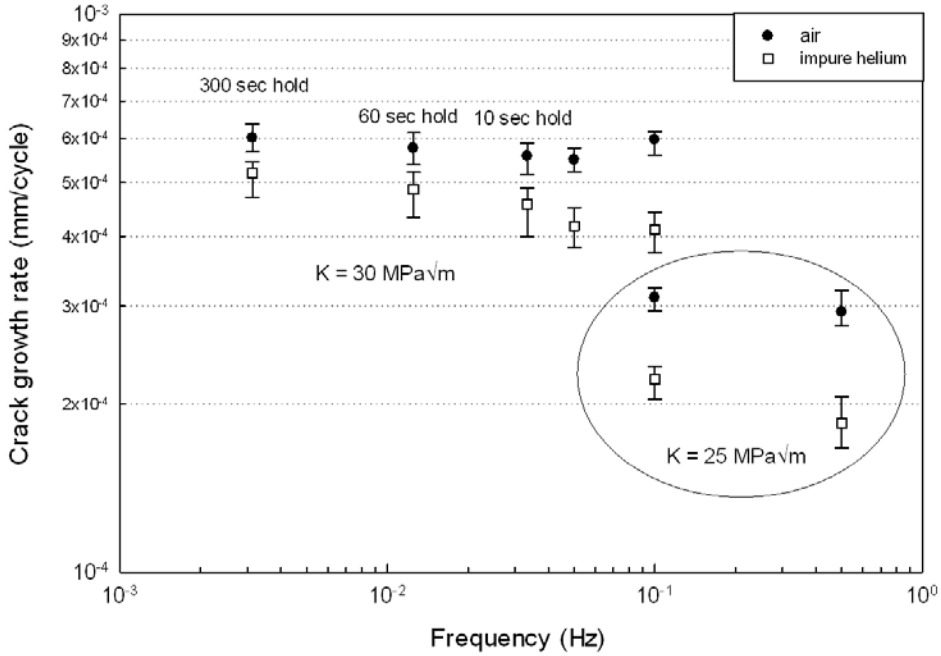


**Figure 39. The fatigue crack growth rates for Inconel 617 at 650 °C. Image courtesy of Julian Benz, Idaho National Laboratory.**

**Table 6. The analysis of variance, ANOVA, results for the testing parameters, and environment**

| Parameter | Conditions | F-ratio | Sig. Level | Sig.[1] |
|---|---|---|---|---|
| Waveform[2] | Tri, Trap | $F(1, 485) = 3.048$ | $p = 0.08$ | n.s. |
| Frequency[3] | 0.01, 0.05 | $F(1, 357) = 0.796$ | $p = 0.37$ | n.s. |
| $K_{max}$[4] | 20, 25, 30 | $F(2,729) = 1.930$ | $p = 0.15$ | n.s. |
| Environment | Im-He, Air | $F(1, 385) = 0.463$ | $p = 0.50$ | n.s. |

[1]n.s. = not significant; [2]"tri" = Triangular, "Trap" = Trapezoidal; [3]Hz [4]MPa√m

influence from the testing parameters or environment on the microstructural aspects of cracking. This apparent contrast suggests that the path of the crack is not influenced by the rate of crack growth during Mode I and II crack propagation. Therefore, it can be assumed that crack propagation was sufficiently slow to be influenced by the microstructure at the crack growth rates seen in this study, which allows for the crack path to show the microstructural effects seen in this study.

The statistics presented in Table 6 confirm that the testing and environmental parameters did not have a significant effect on the crack propagation path. For a result to be significant, a significance level below 0.05 needs to be achieved. All parameters except waveform are much greater than this. However, the waveform does show a weak significance. In further study, it could be found that waveform does hold a greater significance. This is because the small amount of data available for the trapezoidal waveform. If more data points could be collected, there may be a significance found for this waveform. The visually observed behavior in Figure 35 indicates that the fatigue crack propagation character experiences a change toward the end of each crack. It is in this section of the crack that the trapezoidal loading waveform was applied. In this region, the crack has many branches and sharp deviations. Longer hold times at the maximum stress in the loading waveform result in greater change in crack character. Further study is needed with longer sections of the trapezoidal waveform in order to fully elucidate its influence on crack propagation behavior.

### 5.4: Areas of Recrystallization

The recrystallization during fatigue in nickel superalloys has been found in directionally solidified Cobalt-based superalloy [96], directionally solidified Nickel-based superalloys [97], and single crystal Nickel-based superalloys [49, 98-101]. In these studies, it was found that the recrystallization significantly decreases the low cycle fatigue properties of the above materials. Both the fatigue crack initiation and propagation can be accelerated with the occurrences of recrystallized grain boundaries [96]. The study of recrystallization in directionally solidified and single crystal alloys is important in the high temperature application of turbine blades. Research is deficient in

the instance of recrystallization in poly-crystalline superalloys. This can prove to be important in the proposed application in the Very High Temperature Plant and the required service life of 60 years.

Areas of possible recrystallization were identified within the impure-He sample. The question is whether the crack encountered a pocket of pre-existing small grains or if the grains were nucleated during fatigue crack growth. These pockets of grains were found in areas where the crack deviates from the plane of highest stress and were not found in areas where the crack propagated perpendicular to the loading axis. The deviations in crack path occurred close to grain boundaries and between the deviations it propagated close to but not along a general boundary. The resolution of the EBSD data for areas 1 and 2 (Figures 32 and 33) allow for insight into the process. At a step size of 0.1 μm, fine details of the microstructure can be seen. During deformation, the shape and orientation of a grain changes according to the applied stress [68]. Deformation within a grain can be seen as small changes in the lattice orientation within a grain [68, 102, 103]. This deformation can be seen in local misorientation maps such as that found in Figures 32-34. The lack of misorientation within the small grains to either side of the crack suggests that the recrystallization process occurred during the fatigue crack growth. Because of the rarity of the occurrences of the recrystallization along the crack path, further study is needed to determine the conditions in which the recrystallization occurred. Higher resolution, 0.1 μm step size, EBSD scans are needed in order to identify all areas of possible recrystallization.

# CHAPTER SIX: CONCLUSIONS

A study of the influences of microstructure on the propagation of fatigue cracks in Inconel 617 was presented to give further insight into the fatigue crack propagation. In today's society of pushing engineering limits, knowledge gained by developing a deeper understanding into the fatigue process can be used to safely and cost effectively design durable and long lasting components such as the intermediate heat exchanger in the Next Generation Nuclear Plant. This study used electron backscatter diffraction in order to relate the fatigue crack path to that of the microstructure on the scale of microns. Another aspect investigated was the effects of environment and fatigue testing parameters. Two environments were considered, both at 650 °C: lab air and impure-helium, concocted to simulate the conditions within the primary cooling loop in the VHTR. The fatigue crack growth testing parameters considered were: loading waveform (triangular, trapezoidal), loading frequency (0.01, 0.05 Hz), and $K_{max}$ (20, 25, 30 MPa$\sqrt{m}$). The fatigue tests were performed by Julian Benz at Idaho National Laboratory. It was found that the $K_{max}$ had greatest influence in the crack growth rate followed by the testing environment. The following are the key results of this investigation:

- On the microstructural level, the crack has was found to propagate on the {001} family of planes and the <001> to <112> family of directions and has less propensity to propagate in the <111> family of directions. This

supports that crack propagation in Inconel 617 at 650 °C propagates with a ‘quasi-cleavage’ mechanism.

- The character of fatigue crack deflections within a grain versus those at a grain boundary differs with statistical significance. Within a grain, the deflection angle had a unimodal distribution with a mean of 16° ±15°. The low angle of deflection suggests that the plane of highest stress is the highest influencing factor. The deflections at the grain boundary were found to have a different distribution, which was multimodal, suggesting multiple mechanisms for fatigue crack deflection.
- Although the fatigue crack growth rate was found to be highly influenced by the testing atmosphere and parameters, these variables were found to have no statistical significance on the fatigue crack path. At these testing conditions, the crack grew slowly enough for the microstructure to have influence on its path, though it was still constrained to remain close to the plane of highest stress.
- Areas of recrystallized grains were found in the impure-He sample. The lack of local misorientation within these grains suggests that they formed during fatigue crack growth. Further study is needed to determine the conditions in which the recrystallization occurred.

# CHAPTER SEVEN: FUTURE WORK

- Crack propagation angle
    - Apply statistics developed for determination of the five parameters that describe a grain boundary to fully describe the crack plane
    - Perform more testing with the trapezoidal waveform in order to gather insight into its effects on the crack propagation path and/or the crack deviation angle.
- Recrystallization during fatigue
    - More EBSD performed at a fine resolution is needed to find more occurrences of the recrystallization to further describe its mechanism and its influence on fatigue crack propagation.

# REFERENCES


1. Hayner, G.O., et al., *Next Generation Nuclear Plant Materials Research and Development Program Plan,* 2006: Idaho Falls, Idaho.

2. Hwang, J.-J., *Sustainability study of hydrogen pathways for fuel cell vehicle applications.* Renewable and Sustainable Energy Reviews, 2013. **19**: p. 220-229.

3. *INCONEL alloy 617,* S.M. Corporation, Editor 2005.

4. Hosier, J.C. and D.J. Tillack, *Inconel Alloy 617: A New High-Temperature Alloy.* Metals Eng. Quart., 1972. **12**(3): p. 51-55.

5. Jalilian, F., M. Jahazi, and R.A.L. Drew, *Microstructural evolution during transient liquid phase bonding of Inconel 617 using Ni–Si–B filler metal.* Materials Science and Engineering: A, 2006. **423**(1-2): p. 269-281.

6. Mankins, W., J. Hosier, and T. Bassford, *Microstructure and phase stability of INCONEL alloy 617.* Metallurgical and Materials Transactions B, 1974. **5**(12): p. 2579-2590.

7. Cabet, C., et al., *High temperature reactivity of two chromium-containing alloys in impure helium.* Journal of Nuclear Materials, 2008. **375(**2): p. 173-184.

8. Chen, J., P. Rogers, and J. Little, *Oxidation behavior of several chromia-forming commercial nickel-base superalloys.* Oxidation of Metals, 1997. **47**(5): p. 381-410.

9. Haugsrud, R., *On the high-temperature oxidation of nickel.* Corrosion Science, 2003. **45**(1): p. 211-235.

10. Irwin, G.R., *Analysis of stresses and strains near the end of a crack traversing a plate.* J. Appl. Mech., 1957. **24**: p. 361-364.

11. Wei, R.P., *Fracture Mechanics: Integration of Mechanics, Materials Science, and Chemistry* 2010, New York: Cambridge University Press.

12. Rösler, J., H. Harders, and Bäker Martin, *Mechanical behaviour of engineering materials : metals, ceramics, polymers, and composites* 2007, New York: Springer.

13. Griffith, A.A., *The phenomena of rupture and flow in solids.* Philosophical transactions of the royal society of london. Series A, containing papers of a mathematical or physical character, 1921. **221**: p. 163-198.

14. Inglis, C.E., *Stresses in a plate due to the presence of cracks and sharp corners.* Trans. Inst. Naval Architects, 1913. **55**: p. 219-241.

15. Barsom, J., et al., eds. *ASM Handbook, Volume 19 - Fatigue and Fracture*. 1996, ASM International.

16. Paris, P. and F. Erdogan, *A Critical Analysis of Crack Propagation Laws.* Journal of Fluids Engineering, 1963. **85**(4): p. 528-533.

17. Moulin, G., P. Arevalo, and A. Salleo, *Influence of external mechanical loadings (creep, fatigue) on oxygen diffusion during nickel oxidation.* Oxidation of Metals, 1996. **45**(1): p. 153-181.

18. Ghonem, H. and D. Zheng, *Depth of intergranular oxygen diffusion during environment-dependent fatigue crack growth in alloy 718.* Materials Science and Engineering: A, 1992. **150**(2): p. 151-160.

19. Ma, L. and K.-M. Chang, *Identification of SAGBO-induced damage zone ahead of crack tip to characterize sustained loading crack growth in alloy 783.* Scripta Materialia, 2003. **48**(9): p. 1271-1276.

20. Ma, L., X. Liu, and K.-M. Chang, *Reply to comment on "Identification of SAGBO-induced damage zone ahead of crack tip to characterize sustained loading crack growth in alloy 783"*. Scripta Materialia, 2006. **54**(2): p. 309-311.

21. Miller, C.F., G.W. Simmons, and R.P. Wei, *Evidence for internal oxidation during oxygen enhanced crack growth in P/M Ni-based superalloys.* Scripta Materialia, 2003. **48**(1): p. 103-108.

22. Tong, J., et al., *Creep, fatigue and oxidation in crack growth in advanced nickel base superalloys.* International Journal of Fatigue, 2001. **23**(10): p. 897-902.

23. McMahon Jr., C.J., *Comments on "Identification of SAGBO-induced damage zone ahead of crack tip to characterize sustained loading crack growth in alloy 783"*. Scripta Materialia, 2006. **54**(2): p. 305-307.

24. Kaynak, C., A. Ankara, and T.J. Baker, *A comparison of short and long fatigue crack growth in steel.* International Journal of Fatigue, 1996. **18**(1): p. 17-23.

25. Ramsamooj, D.V., *Analytical prediction of short to long fatigue crack growth rate using small- and large-scale yielding fracture mechanics.* International Journal of Fatigue, 2003. **25**(9–11): p. 923-933.

26. Krupp, U., *Fatigue crack propagation in metals and alloys: Microstructural aspects and modelling concepts* 2007, Weinheim Germany: Wiley-VCH.

27. Tokaji, K. and T. Ogawa, *The growth behaviour of microstructurally small fatigue cracks in metals.* Short fatigue cracks, ESIS, 1992. **13**: p. 85-99.

28. Dahal, J., K. Maciejewski, and H. Ghonem, *Loading frequency and microstructure interactions in intergranular fatigue crack growth in a disk Ni-based superalloy.* International Journal of Fatigue.

29. Ghidini, T. and C. Dalle Donne, *Fatigue life predictions using fracture mechanics methods.* Engineering Fracture Mechanics, 2009. **76**(1): p. 134-148.

30. Hour, K. and J. Stubbins, *The effects of hold time and frequency on crack growth in alloy 800H at 650 °C.* Metallurgical and Materials Transactions A, 1989. **20**(9): p. 1727-1734.

31. Vöse, F., et al., *An approach to life prediction for a nickel-base superalloy under isothermal and thermo-mechanical loading conditions.* International Journal of Fatigue. **53**: p. 49-57.

32. Carden, A.E., *A critical evaluation of fatigue crack growth measurement techniques for elevated temperature applications.* Welding Research Council Bulletin, 1983. **283**(11): p. 1-11.

33. Christ, H.-J., *Effect of environment on thermomechanical fatigue life.* Materials Science and Engineering: A, 2007. **468–470**: p. 98-108.

34. Goswami, T. and H. Hanninen, *Dwell effects on high temperature fatigue damage mechanisms: Part II.* Materials & Design, 2001. **22**(3): p. 217-236.

35. Goswami, T. and H. Hänninen, *Dwell effects on high temperature fatigue behavior: Part I.* Materials & Design, 2001. **22**(3): p. 199-215.

36. Kaae, J.L., *High-temperature low-cycle fatigue of Alloy 800H.* International Journal of Fatigue, 2009. **31**(2): p. 332-340.

37. Nilsson, J. and R. Sandstrom, *Influence of Temperature and Microstructure on Creep-Fatigue of Alloy 800H.* High Temperature Technology, 1988. **6**(4): p. 181-186.

38. Rao, B.S., H.P. Meurer, and H. Schuster, *Creep-fatigue interaction of inconel 617 at 950°C in simulated nuclear reactor helium.* Materials Science and Engineering: A, 1988. **104**: p. 37-51.

39. Floreen, S. and R.H. Kane, *An Investigation of the Creep-Fatigue-Environment Interaction in a Ni-Based Superalloy.* Fatigue & Fracture of Engineering Materials & Structures, 1979. **2**(4): p. 401-412.

40. Lenets, Y.N., *Compression fatigue crack growth behavior of metallic alloys: Effect of environment.* Engineering Fracture Mechanics, 1997. **57**(5): p. 527-539.

41. Pineau, A. and S.D. Antolovich, *High temperature fatigue of nickel-base superalloys – A review with special emphasis on deformation modes and oxidation.* Engineering Failure Analysis, 2009. **16**(8): p. 2668-2697.

42. Ruiz-Sabariego, J.A. and S. Pommier, *Oxidation assisted fatigue crack growth under complex non-isothermal loading conditions in a nickel base superalloy.* International Journal of Fatigue, 2009. **31**(11–12): p. 1724-1732.

43. Totemeier, T.C. and H. Tian, *Creep-fatigue–environment interactions in INCONEL 617.* Materials Science and Engineering: A, 2007. **468-470**: p. 81-87.

44. Goswami, T., *Low cycle fatigue—dwell effects and damage mechanisms.* International Journal of Fatigue, 1999. **21**(1): p. 55-76.

45. Rao, K., H. Schuster, and G. Halford, *Mechanisms of high-temperature fatigue failure in alloy 800H.* Metallurgical and Materials Transactions A, 1996. **27**(4): p. 851-861.

46. Yuen, J.L. and P. Roy, *Effect of grain-size on the near threshold fatigue crack-propagation of a nickel-base precipitation hardened superalloy.* Scripta Metallurgica, 1985. **19**(1): p. 17-22.

47. Ferrie, E. and M. Sauzay, *Influence of local crystallographic orientation on short crack propagation in high cycle fatigue of 316LN steel.* Journal of Nuclear Materials, 2009. **386–388**: p. 666-669.

48. Li, L.L., et al., *Effect of crystallographic orientation and grain boundary character on fatigue cracking behaviors of coaxial copper bicrystals.* Acta Materialia, 2013. **61**(2): p. 425-438.

49. Moverare, J.J., S. Johansson, and R.C. Reed, *Deformation and damage mechanisms during thermal–mechanical fatigue of a single-crystal superalloy.* Acta Materialia, 2009. **57**(7): p. 2266-2276.

50. Peralta, P., et al., *Effects of Local Grain Orientation on Fatigue Crack Growth in Multicrystalline fcc Metallic Materials.* Journal of Engineering Materials and Technology, 2005. **127**(1): p. 23-32.

51. Simonovski, I. and L. Cizelj, *The influence of grains' crystallographic orientations on advancing short crack.* International Journal of Fatigue, 2007. **29**(9–11): p. 2005-2014.

52. Gao, Y., et al., *High-cycle fatigue of nickel-base superalloy René 104 (ME3): Interaction of microstructurally small cracks with grain boundaries of known character.* Acta Materialia, 2007. **55**(9): p. 3155-3167.

53. Hansson, P. and S. Melin, *Characteristics of short fatigue crack growth in the vicinity of a low angle grain boundary.* International Journal of Fatigue, 2012. **36**(1): p. 59-67.

54. Kobayashi, S., et al., *Grain boundary engineering for control of fatigue crack propagation in austenitic stainless steel.* Procedia Engineering, 2011. **10**: p. 112-117.

55. Li, L.L., et al., *Higher fatigue cracking resistance of twin boundaries than grain boundaries in Cu bicrystals.* Scripta Materialia, 2011. **65**(6): p. 505-508.

56. Zhang, Z.F. and Z.G. Wang, *Grain boundary effects on cyclic deformation and fatigue damage.* Progress in Materials Science, 2008. **53**(7): p. 1025-1099.

57. Andersson, H. and C. Persson, *In-situ SEM study of fatigue crack growth behaviour in IN718.* International Journal of Fatigue, 2004. **26**(3): p. 211-219.

58. Jono, M., A. Sugeta, and Y. Uematsu, *Atomic force microscopy and the mechanism of fatigue crack growth.* Fatigue & Fracture of Engineering Materials & Structures, 2001. **24**(12): p. 831-842.

59. Akbari-Garakani, M. and M. Mehdizadeh, *Effect of long-term service exposure on microstructure and mechanical properties of Alloy 617.* Materials & Design, 2011. **32**(5): p. 2695-2700.

60. Schlegel, S., et al., *Precipitate Redistribution during Creep of Alloy 617.* Metallurgical and Materials Transactions A, 2009. **40**(12): p. 2812-2823.

61. Kewther Ali, M., M.S.J. Hashmi, and B.S. Yilbas, *Fatigue properties of the refurbished INCO-617 alloy.* Journal of Materials Processing Technology, 2001. **118**(1–3): p. 45-49.

62. Kim, D., I. Sah, and C. Jang, *Effects of high temperature aging in an impure helium environment on low temperature embrittlement of Alloy 617 and Haynes 230.* Journal of Nuclear Materials, 2010. **405**(1): p. 9-16.

63. Schwartz, A.J., *Electron backscatter diffraction in materials science*. 2nd ed 2009, New York: Springer.

64. Klimek, L. and B. Pietrzyk, *Electron backscatter diffraction as a useful method for alloys microstructure characterization.* Journal of Alloys and Compounds, 2004. **382**(1): p. 17-23.

65. Britton, T. and A. Wilkinson, *Measurement of residual elastic strain and lattice rotations with high resolution electron backscatter diffraction.* Ultramicroscopy, 2011. **111**(8): p. 1395-1404.

66. Child, D.J., G.D. West, and R.C. Thomson, *The use of combined three-dimensional electron backscatter diffraction and energy dispersive X-ray analysis to assess the characteristics of the gamma/gamma-prime microstructure in alloy 720Li™.* Ultramicroscopy, 2012. **114**: p. 1-10.

67. Deal, A., T. Hooghan, and A. Eades, *Energy-filtered electron backscatter diffraction.* Ultramicroscopy, 2008. **108**(2): p. 116-125.

68. Humphreys, F.J., *Review: Grain and subgrain characterisation by electron backscatter diffraction.* Journal of Materials Science, 2001. **36**(16): p. 3833-3854.

69. Kamaya, M., *Measurement of local plastic strain distribution of stainless steel by electron backscatter diffraction.* Materials Characterization, 2009. **60**(2): p. 125-132.

70. Randle, V., *Applications of electron backscatter diffraction to materials science: status in 2009.* Journal of Materials Science, 2009. **44**(16): p. 4211-4218.

71. Baba-Kishi, K.Z., *Review Electron backscatter Kikuchi diffraction in the scanning electron microscope for crystallographic analysis.* Journal of Materials Science, 2002. **37**(9): p. 1715-1746.

72. Nishikawa, S. and S. Kikuchi, *The diffraction of cathode rays by calcite.* Proc Imerial Acad (Japan), 1928. **4**: p. 475-477.

73. De Graef, M. and M.E. McHenry, *Structure of materials: An introduction to crystallography, diffraction and symmetry* 2007, New York: Cambridge University Press.

74. Lassen, K., *Automatic high-precision measurements of the location and width of Kikuchi bands in electron backscatter diffraction patterns.* Journal of Microscopy, 1998. **190**(3): p. 375-391.

75. Nowell, M.M. and S.I. Wright, *Orientation effects on indexing of electron backscatter diffraction patterns.* Ultramicroscopy, 2005. **103**(1): p. 41-58.

76. Jazaeri, H. and F. Humphreys, *Quantifying recrystallization by electron backscatter diffraction.* Journal of Microscopy, 2004. **213**(3): p. 241-246.

77. Amelinckx, S. and W. Dekeyser, *The Structure and Properties of Grain Boundaries*, in *Solid State Physics*, S. Frederick and T. David, Editors. 1959, Academic Press. p. 325-499.

78. Weinberg, F., *Grain boundaries in metals.* Progress in Metal Physics, 1959. **8**: p. 105-146.

79. Palumbo, G., et al., *On a More Restrictive Geometric Criterion for "Special" CSL Grain Boundaries.* Scripta Materialia, 1998. **38**(11): p. 1685-1690.

80. Randle, V. and H. Davies, *A comparison between three-dimensional and two-dimensional grain boundary plane analysis.* Ultramicroscopy, 2002. **90**(2–3): p. 153-162.

81. Saylor, D., et al., *Measuring the five-parameter grain-boundary distribution from observations of planar sections.* Metallurgical and Materials Transactions A, 2004. **35**(7): p. 1981-1989.

82. Randle, V., *The coincidence site lattice and the 'sigma enigma'*. Materials Characterization, 2001. **47**(5): p. 411-416.

83. Shimada, M., et al., *Optimization of grain boundary character distribution for intergranular corrosion resistant 304 stainless steel by twin-induced grain boundary engineering.* Acta Materialia, 2002. **50**(9): p. 2331-2341.

84. Shvindlerman, L.S. and B.B. Straumal, *Regions of existence of special and non-special grain boundaries.* Acta Metallurgica, 1985. **33**(9): p. 1735-1749.

85. Brandon, D.G., *The structure of high-angle grain boundaries.* Acta Metallurgica, 1966. **14**(11): p. 1479-1484.

86. Déchamps, M., F. Baribier, and A. Marrouche, *Grain-boundaries: Criteria of specialness and deviation from CSL misorientation.* Acta Metallurgica, 1987. **35**(1): p. 101-107.

87. Salkind, N.J., *Statistics for people who (think they) hate statistics*. 4th ed 2011, Thousand Oaks: SAGE Publications.

88. Devore, J.L., *Probability and statistics for engineering and the sciences*. 7th ed 2008, Belmont, CA: Thomson/Brooks/Cole.

89. Sahm, P.R., M.O. Speidel, and Brown Boveri Research Center., *High-temperature materials in gas turbines : proceedings of the Symposium on High-temperature Materials in Gas Turbines, Brown, Boveri & Company Limited, Baden, Switzerland, 1973* 1974, Amsterdam ; New York: Elsevier Scientific Pub. Co. xx, 388 p. with ill.

90. Sadananda, K. and P. Shahinian, *Analysis of crystallographic high temperature fatigue crack growth in a nickel base alloy.* Metallurgical Transactions A, 1981. **12**(2): p. 343-351.

91. Arakere, N.K., *High-temperature fatigue properties of single crystal superalloys in air and hydrogen.* Journal of engineering for gas turbines and power, 2004. **126**(3): p. 590-603.

92. Leo Prakash, D.G., et al., *Crack growth micro-mechanisms in the IN718 alloy under the combined influence of fatigue, creep and oxidation.* International Journal of Fatigue, 2009. **31**(11–12): p. 1966-1977.

93. Yoder, G., L. Cooley, and T. Crooker, *Fatigue crack propagation resistance of beta-annealed Ti-6AI-4V alloys of differing interstitial oxygen contents.* Metallurgical Transactions A, 1978. **9**(10): p. 1413-1420.

94. Henderson, M. and J. Martin, *The influence of crystal orientation on the high temperature fatigue crack growth of a Ni-based single crystal superalloy.* Acta Materialia, 1996. **44**(1): p. 111-126.

95. Kundu, T., *Fundamentals of fracture mechanics* 2008, Boca Raton, FL: CRC Press.

96. Zhao, Y., et al., *Effects of recrystallization on the low cycle fatigue behavior of directionally solidified superalloy DZ40M.* Rare Metals, 2008. **27**(4): p. 425-428.

97. Xie, G., J. Zhang, and L.-h. Lou, *Effect of cyclic recovery heat treatment on surface recrystallization of a directionally solidified superalloy.* Progress in Natural Science: Materials International, 2011. **21**(6): p. 491-495.

98. Wu, Y.-x., et al., *Kinetics and microstructural evolution during recrystallization of a Ni3Al-based single crystal superalloy.* Transactions of Nonferrous Metals Society of China, 2012. **22**(9): p. 2098-2105.

99. Moverare, J.J. and S. Johansson, *Damage mechanisms of a high-Cr single crystal superalloy during thermomechanical fatigue.* Materials Science and Engineering: A, 2010. **527**(3): p. 553-558.

100. He, Y.H., et al., *Recrystallization and fatigue fracture of single crystal turbine blades.* Engineering Failure Analysis, 2011. **18**(3): p. 944-949.

101. Xiong, J.C., et al., *Effects of carburization on recrystallization behavior of a single crystal superalloy.* Materials Characterization, 2010. **61**(7): p. 749-755.

102. Jorge-Badiola, D., A. Iza-Mendia, and I. Gutiérrez, *Study by EBSD of the development of the substructure in a hot deformed 304 stainless steel.* Materials Science and Engineering: A, 2005. **394**(1–2): p. 445-454.

103. M'Saoubi, R. and L. Ryde, *Application of the EBSD technique for the characterisation of deformation zones in metal cutting.* Materials Science and Engineering: A, 2005. **405**(1): p. 339-349.